



**HAL**  
open science

# A new treatment of telluric and stellar features for medium-resolution spectroscopy and molecular mapping

F. Kiefer, M. Bonnefoy, B. Charnay, A. Boccaletti, A.-M. Lagrange, G. Chauvin, B. Bézard, M. Mâlin

## ► To cite this version:

F. Kiefer, M. Bonnefoy, B. Charnay, A. Boccaletti, A.-M. Lagrange, et al.. A new treatment of telluric and stellar features for medium-resolution spectroscopy and molecular mapping. *Astronomy and Astrophysics - A&A*, 2024, 685, pp.A120. 10.1051/0004-6361/202347068 . hal-04575428

**HAL Id: hal-04575428**

**<https://hal.science/hal-04575428v1>**





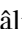

Submitted on 14 May 2024

**HAL** is a multi-disciplinary open access archive for the deposit and dissemination of scientific research documents, whether they are published or not. The documents may come from teaching and research institutions in France or abroad, or from public or private research centers.

L'archive ouverte pluridisciplinaire **HAL**, est destinée au dépôt et à la diffusion de documents scientifiques de niveau recherche, publiés ou non, émanant des établissements d'enseignement et de recherche français ou étrangers, des laboratoires publics ou privés.

# A new treatment of telluric and stellar features for medium-resolution spectroscopy and molecular mapping

## Application to the abundance determination on $\beta$ Pic b

F. Kiefer<sup>1</sup> , M. Bonnefoy<sup>2</sup> , B. Charnay<sup>1</sup> , A. Boccaletti<sup>1</sup>, A.-M. Lagrange<sup>1,2</sup>, G. Chauvin<sup>3,2</sup> ,  
B. Bézard<sup>1</sup> , and M. Mâlin<sup>1</sup> 

<sup>1</sup> LESIA, Observatoire de Paris, Université PSL, CNRS, Sorbonne Université, Université Paris Cité, 5 place Jules Janssen, 92195 Meudon, France

e-mail: flavien.kiefer@obspm.fr

<sup>2</sup> Univ. Grenoble Alpes, CNRS, IPAG, 38000 Grenoble, France

<sup>3</sup> Laboratoire Lagrange, Université Côte d'Azur, CNRS, Observatoire de la Côte d'Azur, 06304 Nice, France

Received 1 June 2023 / Accepted 11 February 2024

### ABSTRACT

Molecular mapping is a supervised method exploiting the spectral diversity of integral field spectrographs to detect and characterise resolved exoplanets blurred into the stellar halo. We present an update to the method, aimed at removing the stellar halo and the nuisance of telluric features in the datacubes and accessing a continuum-subtracted spectra of the planets at  $R \sim 4000$ . We derived the planet atmosphere properties from a direct analysis of the planet telluric-corrected absorption spectrum. We applied our methods to the SINFONI observation of the planet  $\beta$  Pictoris b. We recovered the CO and H<sub>2</sub>O detections in the atmosphere of  $\beta$  Pic b by using molecular mapping. We further determined some basic properties of its atmosphere, with  $T_{\text{eq}}=1748^{+3}_{-4}$  K, sub-solar  $[\text{Fe}/\text{H}]=-0.235^{+0.015}_{-0.013}$  dex, and solar  $\text{C}/\text{O}=0.551\pm 0.002$ . These results are in contrast to values measured for the same exoplanet with other infrared instruments. We confirmed a low projected equatorial velocity of  $25^{+5}_{-6}$  km s<sup>-1</sup>. We were also able to measure, for the first time and with a medium-resolution spectrograph, the radial velocity of  $\beta$  Pic b relative to the central star at MJD=56910.38 with a km s<sup>-1</sup> precision of  $-11.3\pm 1.1$  km s<sup>-1</sup>. This result is compatible with the ephemerides, based on the current knowledge of the  $\beta$  Pic system.

**Key words.** techniques: imaging spectroscopy – planets and satellites: atmospheres – planets and satellites: composition – planets and satellites: formation – planets and satellites: gaseous planets – planets and satellites: individual: beta Pictoris b

## 1. Introduction

The system of  $\beta$  Pictoris, with its imaged debris disk of dust, evaporating exocomets and two giant planets, opens a stunning window into early stages of planetary systems formation and evolution. At the age of  $\beta$  Pic  $\sim 23\pm 3$  Myr (Mamajek & Bell 2014), giant planets have already formed, most of the protoplanetary gas has disappeared from the disk, and Earth-mass planets may be still forming. The discovery of  $\beta$  Pic b in direct high-contrast imaging (Lagrange et al. 2009) was rapidly recognised as a major finding for several reasons. First, until the discoveries of  $\beta$  Pic c (Lagrange et al. 2019; Nowak et al. 2020) and, more recently, AF Lep b (Mesa et al. 2023), it was the shortest period imaged exoplanet, thus enabling a ‘fast’ orbital characterisation. Second, once its mass is known, it can be used to calibrate brightness-mass models and atmosphere models at young ages. Third, it serves as a precious benchmark for detailed atmosphere and physical characterisations, thanks to its proximity to Earth and position with respect to the star. Finally, it is an exquisite laboratory for studying disk-planet interactions at a post-transition disk stage (Lagrange et al. 2010, 2012).

Model- and age-dependent brightness-mass relationships predict  $\beta$  Pic b mass to be within 9–13  $M_{\text{J}}$  (Bonnefoy et al. 2013; Morzinski et al. 2015; Chilcote et al. 2017). Its mass is still marginally constrained observationally because of significant uncertainties on the amplitude of the radial velocities (RV)

variations induced by the planets b and c. In particular, the available RV data do not cover the whole  $\beta$  Pic b period, the extrema of the recently discovered  $\beta$  Pic c-induced variations are not well constrained with the available data, while the RV variations are strongly dominated by the stellar pulsations (see examples in Lagrange et al. 2019, 2020; Vandal et al. 2020). *Gaia* data were used by several authors to further constrain the planet b mass:  $<20 M_{\text{J}}$  (Bonnefoy et al. 2013),  $13\pm 3 M_{\text{J}}$  (Dupuy et al. 2019),  $12.7\pm 2.2 M_{\text{J}}$  (GRAVITY Collaboration 2020), and  $10\text{--}11 M_{\text{J}}$  (Lagrange et al. 2020). The most recent determinations combine RV, relative and absolute astrometry, taking into account both planets b and c. They lead to  $9.3^{+2.6}_{-2.5} M_{\text{J}}$  using the HIPPARCOS–*Gaia* DR2 measurement of astrometric acceleration (Brandt et al. 2021), and  $11.7^{+2.3}_{-2.1} M_{\text{J}}$  using the HIPPARCOS–*Gaia* DR3 measurement of astrometric acceleration with the same datasets (Feng et al. 2022). We note that the astrometric acceleration measurement, also known as proper motion anomaly (see also Kervella et al. 2019, 2022), initially  $2.54\text{--}\sigma$  significant using the DR2 (Kervella et al. 2019), became compatible with zero at  $0.86\text{--}\sigma$  using the DR3 (Kervella et al. 2022). This explains the difference in the derived mass. From dynamical considerations, the mass of  $\beta$  Pic b is thus bounded within 9–15  $M_{\text{J}}$ .

The study of infrared spectra emitted by transiting and non-transiting hot Jupiter (Brogi et al. 2012, 2013, 2014; de Kok et al. 2013; Birkby et al. 2013, 2017; Lockwood et al. 2014;

Piskorz et al. 2016, 2017; Guilluy et al. 2019; Cont et al. 2021, 2022a,b; Yan et al. 2022) and young imaged planets (Snellen et al. 2014; Brogi et al. 2018; Hoeijmakers et al. 2018; Petit dit de la Roche et al. 2018; Ruffio et al. 2019, 2021; GRAVITY Collaboration 2020; Cugno et al. 2021; Petrus et al. 2021; Patapis et al. 2022; Petrus et al. 2023; Mâlin et al. 2023; Miles et al. 2023; Landman et al. 2023) allows us to characterise the atmospheric composition in molecules such as CO, CO<sub>2</sub>, H<sub>2</sub>O, NH<sub>3</sub>, and CH<sub>4</sub>. The molecular mapping method was first developed for this objective by Snellen et al. (2014), hereafter S14, for medium- or high-resolution instruments such as CRIRES (S14, Landman et al. 2023), SINFONI (Hoeijmakers et al. 2018; Cugno et al. 2021; Petrus et al. 2021), Keck/OSIRIS (Petit dit de la Roche et al. 2018; Ruffio et al. 2019, 2021), or JWST/MRS (Patapis et al. 2022; Mâlin et al. 2023; Miles et al. 2023). This method consists in calculating the cross-correlation function (CCF) of a spectrum emitted from the atmosphere of a planet with a theoretical transmission spectrum, or template, using for instance Exo-REM (Baudino et al. 2015; Charnay et al. 2018). This could reveal the presence of individual molecules. The CCF leads to a similarity score, which if equal to 1 (0) means the spectrum and the template are proportional (totally orthogonal). In general, because of noise, systematics, and inaccuracies of models, a CCF never reaches exactly 1. Using the CCF as a template matching score in principle allows us to retrieve simple atmospheric properties such as  $T_{\text{eff}}$ ,  $\log g$ , and relative abundances.

For  $\beta$  Pic b, Hoeijmakers et al. (2018, H18 hereafter) showed using molecular mapping on the cubes collected by the Spectrograph for INtegral Field Observations in the Near Infrared (or SINFONI) that H<sub>2</sub>O and CO were present in the atmosphere of this young planet, with no evidence of other species. They did a tentative template matching of  $T_{\text{eff}}$  and  $\log g$  that led only to large confidence regions of those parameters on their Fig. 10. They did not produce any estimation of the planet radial velocity, nor the rotational broadening,  $v \sin i$ .

With a spectrum-fitting oriented approach, an emitted spectrum of  $\beta$  Pic b was obtained with GRAVITY (GRAVITY Collaboration 2020). Its fit led, in a Bayesian inference framework using Markov chain Monte Carlo sampling of posteriors, to an effective temperature of  $1740 \pm 10$  K with  $\log g = 4.35 \pm 0.09$ , a super-solar metallicity of  $[M/H] \sim 0.7 \pm 0.1$  and a sub-solar C/O =  $0.43 \pm 0.04$ <sup>1</sup>. This was in good agreement with previous estimations of the planet temperature of 1724 K and a  $\log g = 4.2$  by Chilcote et al. (2017) and the combined astrometric+RV planet mass estimation  $\sim 12 M_J$  (Snellen & Brown 2018; GRAVITY Collaboration 2020; Lagrange et al. 2020). However, the metallicity was significantly different if considering the GRAVITY spectrum only ( $-0.5$  dex) or combined with the GPI YJH low-resolution spectra ( $>0.5$  dex). Most recently, Landman et al. (2023) published the analysis of new  $\beta$  Pic b high-resolution spectra taken with the upgraded CRIRES+ instrument that led to similar parameters using atmospheric retrievals, with temperatures slightly higher than in GRAVITY Collaboration (2020), a sub-solar metallicity ( $\text{Fe}/\text{H} \sim -0.4$ ) and a sub-solar C/O =  $0.41 \pm 0.04$ . Thanks to the high resolution of the instrument, they were able to obtain a new  $v \sin i$  measurement of  $19.9 \pm 1.1 \text{ km s}^{-1}$ .

Using an approach similar to that of GRAVITY Collaboration (2020), Petrus et al. (2021) used both a principal component analysis (PCA) and halo-subtraction on

north-aligned angular differential imaging (nADI) on SINFONI observations of HIP 65426 to extract the emitted spectrum of the planet *b* keeping the thermal continuum. They then used Bayesian inference with nested sampling (Skilling 2006) to retrieve the basic parameters of planet HIP 65426 b from the spectrum itself, including equilibrium temperature, surface gravity, metallicity ratio  $[M/H]$ , and C/O. This demonstrated that it was possible to derive the spectrum of a planet observed with SINFONI and that having a spectrum-fitting, rather than CCF-optimisation method, leads to more reliable results.

In this work, we performed a new analysis of the  $\beta$  Pic cubes observed with SINFONI. We improved the reduction of the cubes, as explained in Sect. 2. We then improved the star removal method used by H18 with a different approach, which corrects for residuals from the stellar lines. We discuss the H18 method and explain our improvements in the form of a new method called *starem* in Sect. 3.2. Then, in Sect. 4, we apply a molecular mapping and compare it to the H18 results. We further extract the spectrum of the planet in Sect. 5. We use a simple grid search as well as a Bayesian framework with an MCMC sampling to fit the observed planet spectrum and measure the parameters of the planet. This is done in Sect. 6. We discuss the results in Sect. 7 and give our conclusions in Sect. 8.

## 2. SINFONI data pre-processing

### 2.1. SINFONI observations

SINFONI was an infrared instrument, coupling an adaptive optics (AO) module to an integral field spectrograph (IFS) SPIFFI, installed on the Unit Telescope 4 of the Very Large Telescope at Paranal/Chile (Eisenhauer et al. 2003; Bonnet et al. 2004). SINFONI was on-sky from 2004 to 2019. Observations with the SINFONI IFS were performed with different sizes for the field-of-view (FoV) and spectral resolution ( $R$ ), then reduced into data cubes, with two spatial and one spectral dimensions. Here, we focus on observations of the  $\beta$  Pictoris surroundings performed with the  $0.8'' \times 0.8''$  FoV subdivided into  $64 \times 64$  spaxels<sup>2</sup> of size  $12.5 \times 12.5 \text{ mas}^2$  at  $R=4000$  along the *K*-band ( $2.08\text{--}2.45 \mu\text{m}$ ). The observations consist in 24 exposures of 60 s each, recorded on the 10th September 2014 from 08:19:34 UT to 10:05:20 UT. An offset of  $0.9\text{--}1.1''$  from  $\beta$  Pic and a field rotation of  $-56^\circ$  to  $-19^\circ$  was applied, reducing the pollution of the stellar halo upon the planet spaxels with the star decentred outside the FoV, focusing the observations on the surroundings of  $\beta$  Pictoris, and enabling the use of angular differential imaging (Marois et al. 2006). The seeing during the observation varied within  $0.8\text{--}1.0''$  with an airmass varying from 1.35 to 1.14 between the first and the last exposure. The atmospheric conditions were relatively constant during the observations, with fluctuations of pressure and temperature of  $<1\%$ .

### 2.2. From SINFONI raw data to registered cubes

We performed the data reduction of the SINFONI sequence of observations following the scheme described in Petrus et al. (2021), which provides optimally-reduced datacubes for high-contrast science.

The raw data were originally corrected the Toolkit for Exoplanet deTectioN and chaRacterisation with IfS (hereafter,

<sup>1</sup> The commonly adopted solar abundance values are  $\log N_{\text{M},\odot}/N_{\text{H},\odot} = \log Z_{\odot}/X_{\odot} = -1.74$  and C/O = 0.55 (Asplund et al. 2009).

<sup>2</sup> Initially, there were  $64 \times 32$  rectangular spaxels of a size of  $12.5 \times 25 \text{ mas}^2$ , but they were then subdivided into  $64 \times 64$  square spaxels by splitting one spaxel into two equal flux spaxels.

TE<sub>x</sub>TRIS; Petrus et al. 2021; Palma-Bifani et al. 2023; Demars et al. 2023, Bonnefoy et al., in prep.) from the so-called ‘odd-even’ effect affecting randomly some pre-amplification channels on SPIFFI’s detector (corresponding roughly to the location of the 25th slitlet). We then used the ESO data handling pipeline version 3.0.0 to reconstruct data cubes from the bi-dimensional science frames. TE<sub>x</sub>TRIS also corrected for the improper registration of the slitlet edges on the detector and for the inaccurate wavelength solution found by the pipeline using synthetic spectra of the telluric absorptions.

Finally, we used TE<sub>x</sub>TRIS to perform a proper registration of the star position outside the field of view. H18 fitted a synthetic function to represent the wings of the star’s point spread function (PSF). However, such a method is sensitive to the distribution of flux within the FoV. The later can be affected by (i) the complex evolution of the Strehl ratio that evolved with wavelength and along the sequence, cubes with high Strehl ratios, showing strong artefacts due to the telescope spiders (while those with low Strehl ratio show a smoother flux distribution) and (ii) the varying part of the halo contained in the FoV due to the field rotation along the sequence. TE<sub>x</sub>TRIS uses instead an initial measurement of the star position in data cubes acquired during short exposures taken at the beginning of the sequence and centred on the star. Then it builds a model of the  $\beta$  Pic centroid positions, which are located outside the FoV in the 24 exposures of the observation sequence, by computing their theoretical wavelength-dependent evolution due to the evolving refraction, the field rotation, and the offsets on sky.

A remaining error due to telescope flexure exists (see the ESO user manual) but appears to be below  $\sim 1$  pixel in the final registered cubes of  $\beta$  Pictoris. This reduction provides us with 24 data cubes and associated measurements of the offsets and rotation angles that will be used in Sect. 2.5 to de-rotate and stack the cubes aligned on the position of the planet  $\beta$  Pic b.

### 2.3. Reference stellar spectrum

First, we define the method we used throughout this study to derive a reference stellar spectrum, free from photons coming from the planet, in the  $K$ -band using a SINFONI data cube. We found it best to use several of the brightest spaxels within a cube and combine them to obtain a stellar spectrum to reduce any pollution from the background and the planet. To find those, for all spaxels of the FoV, we measured the flux at the continuum-level of the Br- $\gamma$  line at  $\sim 2.165 \mu\text{m}$  by fitting the wings of the line by a two-degree polynomial and retrieving the level of the continuum at  $2.165 \mu\text{m}$ . From this flux map, we excluded the 10 brightest spaxels to avoid bad spaxels and calculated an average star spectrum from the next 100 brightest ones. Those are the less affected by the background whose level is on the order of  $\sim 20 \text{ erg s}^{-1} \text{ cm}^{-2} \text{ \AA}^{-1}$  while the total flux reaches more than  $2000 \text{ erg s}^{-1} \text{ cm}^{-2} \text{ \AA}^{-1}$ . Therefore, its contribution is less than 1% in those spaxels. Figure 1 shows the absolute total and residual flux distribution among spaxels of the stacked cube obtained in Sect. 2.5 below. The resulting reference star spectrum is showed on Fig. 2. We note that it includes many telluric lines beyond  $2.18 \mu\text{m}$ , mainly  $\text{H}_2\text{O}$ ,  $\text{CO}_2$ , and  $\text{CH}_4$  lines.

### 2.4. Wavelength calibration correction

The presence of telluric lines is a nuisance to the analysis of stellar and exoplanet spectra. Nonetheless, they can also be used to adjust the wavelength calibration in the SINFONI cubes.

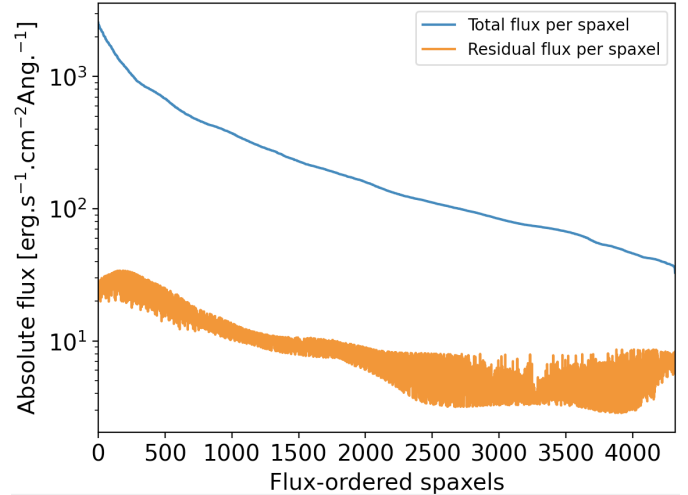


**Fig. 1.** Absolute total (blue) and residual (orange) flux per spaxel. The spaxels are ordered from the brightest to the faintest in absolute total flux per spaxel. The absolute total flux is the raw flux obtained as output of the stack phase in Sect. 2.5. The residual flux is the remaining absolute flux once the star spectrum is removed (see Sect. 3.2 for more details).

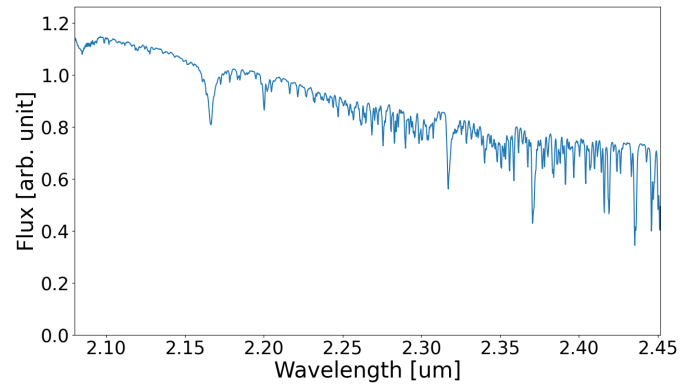


**Fig. 2.** Star spectrum calculated from the brightest spaxels. The flux is normalised to the pseudo-continuum flux at the top of the Br- $\gamma$  line at  $2.165 \mu\text{m}$ .

Tellurics can be fitted directly in each of the 24 cubes to the normalised star spectrum. Since we are most interested in the planet, the star spectrum is here obtained from the spaxels located at the position of the planet. The planet position in the derotated cube is determined in Sect. 4.2 and its PSF of the four-spaxel FWHM in Sect. 3.2. We calculated for each cube the mean stellar spectrum on a circular area of six-spaxel radius around the planet location.

We used the ESO code *molecfit* (Smette et al. 2015; Kausch et al. 2015) v3.13.6 that implements LBLRTM to perform the telluric line fit in this spectrum. Typical site parameters during the observations are taken as inputs, such as the MJD, paranal altitude and coordinates, humidity ( $\sim 4\%$ ), ambient pressure ( $\sim 740 \text{ hPa}$ ), ambient temperature ( $\sim 12^\circ\text{C}$ ), mirror temperature ( $\sim 10.9^\circ\text{C}$ ), and airmass ( $\sec z \sim 1.1\text{--}1.4$ ). *molecfit* fits the atmospheric parameters (such as water column abundance, pressure, temperature, and so on) as well as a continuum, a Chebychev polynomial wavelength solution, and a line spread function to the observed telluric lines in the observed spectrum. The error bars are fixed to the square root of the flux divided by the normalisation. The observed reduced  $\chi^2$  are consistent

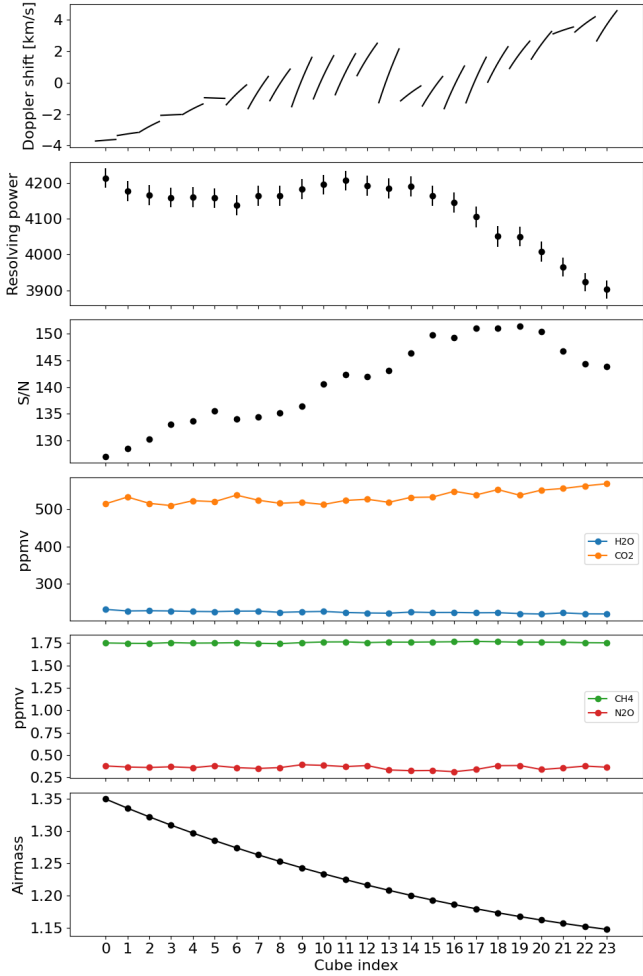


**Fig. 3.** Summary of *molecfit* results. First panel: wavelength solutions showing the Doppler shift against the wavelength through the *K*-band with respect to cubes series number. Second panel: measured resolving power from FWHM of the fitted LSF. Third and fourth panels: fitted ppmv abundances of H<sub>2</sub>O, CO<sub>2</sub>, CH<sub>4</sub>, and N<sub>2</sub>O.

within 1.3–1.4 all through the cubes time series. We found that the molecules H<sub>2</sub>O, CO<sub>2</sub>, CH<sub>4</sub>, and N<sub>2</sub>O dominate the model tellurics spectrum in the *K*-band, whilst CO, NH<sub>3</sub>, O<sub>2</sub>, and O<sub>3</sub> are always either weak and undetermined or fitted to negligible relative abundance values  $<10^{-4}$ . To reduce the computation effort, we thus only fit for H<sub>2</sub>O, CO<sub>2</sub>, CH<sub>4</sub>, and N<sub>2</sub>O column densities. A polynomial of a degree of 6 for the fit of the continuum and of degree of 1 for the fit of the wavelength solution was adopted. We fixed the LSF to a Gaussian function, allowing its width to vary. The LSF is moreover convolved in *molecfit* by a 1-pixel (0.00025  $\mu\text{m}$ ) box to mimic the effect of the slit smearing.

Figure 3 shows a summary of the *molecfit* solutions along the cubes. Figure 4 shows the  $\beta$  Pic stellar spectrum compared with the *molecfit* resulting model. There is a residual time-dependent shift of the wavelength solution even after the absolute calibration performed by TexTRIS of about  $8 \text{ km s}^{-1}$  from first (cube 0) to last (cube 23) exposure. This agrees with the magnitude of the error on the calibration found in Petrus et al. (2021). Such shift could be due to an effect of flexure of the instrument. We corrected the wavelength solution in all cubes according to this analysis. The figure also shows that the resolving power is varying through the observation series with an LSF FWHM of  $\sim 2.16\text{--}2.32$  pixels at  $2.27 \mu\text{m}$ . This variation is due

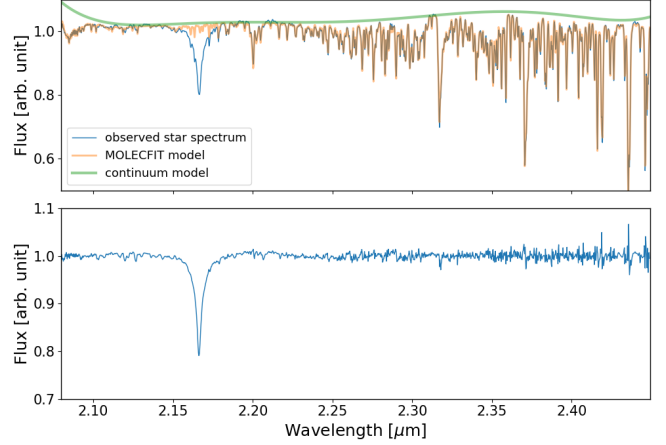


**Fig. 4.** Stellar spectrum observed with SINFONI (blue) compared to the model Earth telluric spectrum calculated with *molecfit* (orange) and the continuum model (green). Upper panel: two spectra compared directly. Lower panel: stellar spectrum divided by the telluric spectrum model.

to the wandering of the planet image on the detector. This leads to an average effective resolving power in our SINFONI *K*-band spectra of  $R=4120\pm 90$ .

The atmospheric molecular column density of H<sub>2</sub>O is relatively constant along the observation sequence. We note that the CO<sub>2</sub> abundance level of  $\sim 500$  ppmv retrieved is  $\sim 1.4$  times higher than the reference value ( $\sim 370$  ppmv) in the model Earth atmosphere, while N<sub>2</sub>O abundance  $\sim 0.30$  ppmv is about 1.2 its reference level. At the same date and using the whole *K*-band spectrum (including deep CO<sub>2</sub> and N<sub>2</sub>O lines below  $2.07 \mu\text{m}$ ) of another reference star, the CO<sub>2</sub>, and N<sub>2</sub>O abundances reach  $\sim 390$  ppmv and  $0.23$  ppmv, respectively (Smette, priv. comm.). Relying on weak lines only, our determination of the CO<sub>2</sub> and N<sub>2</sub>O abundance levels might not be well determined. The absolute values of the species abundances presented here should thus be considered as indicative only.

Applying the same procedure on the star spectrum taken from other locations in the image led to similar molecular abundances. However, it revealed a strongly scattered resolving power within 3500–4900, though the average value of  $R$  agreed on an effective resolving power of  $\sim 4000$ . This is much smaller than the theoretical  $R=5950$ , expected for SINFONI in this setup. This might be explained by the degradation due to pixelation when creating the cubes, since the LSF sampling is sub-Nyquist, with a spectral broadening of about 1.5 pixels as noted in the latest SINFONI’s documentation<sup>3</sup>.

A thorough investigation on how to improve the effective spectral resolution in the reduced data of instruments such as SINFONI is not in the scope of the present study. Nevertheless, with regard to such objective, two leads might be worth mentioning: (i) achieving a finer reconstruction of cubes from the 2D images of the slitlets and the arc lamp calibration, or more simply, yet at the expense of time, or (ii) using dithering during the observations to better sample the LSF, at the cost of at least doubling the exposure time. These leads will be explored in further studies.

<sup>3</sup> <https://www.eso.org/sci/facilities/paranal/decommissioned/sinfoni/doc/VLT-MAN-ESO-14700-3517-P103.1.pdf>

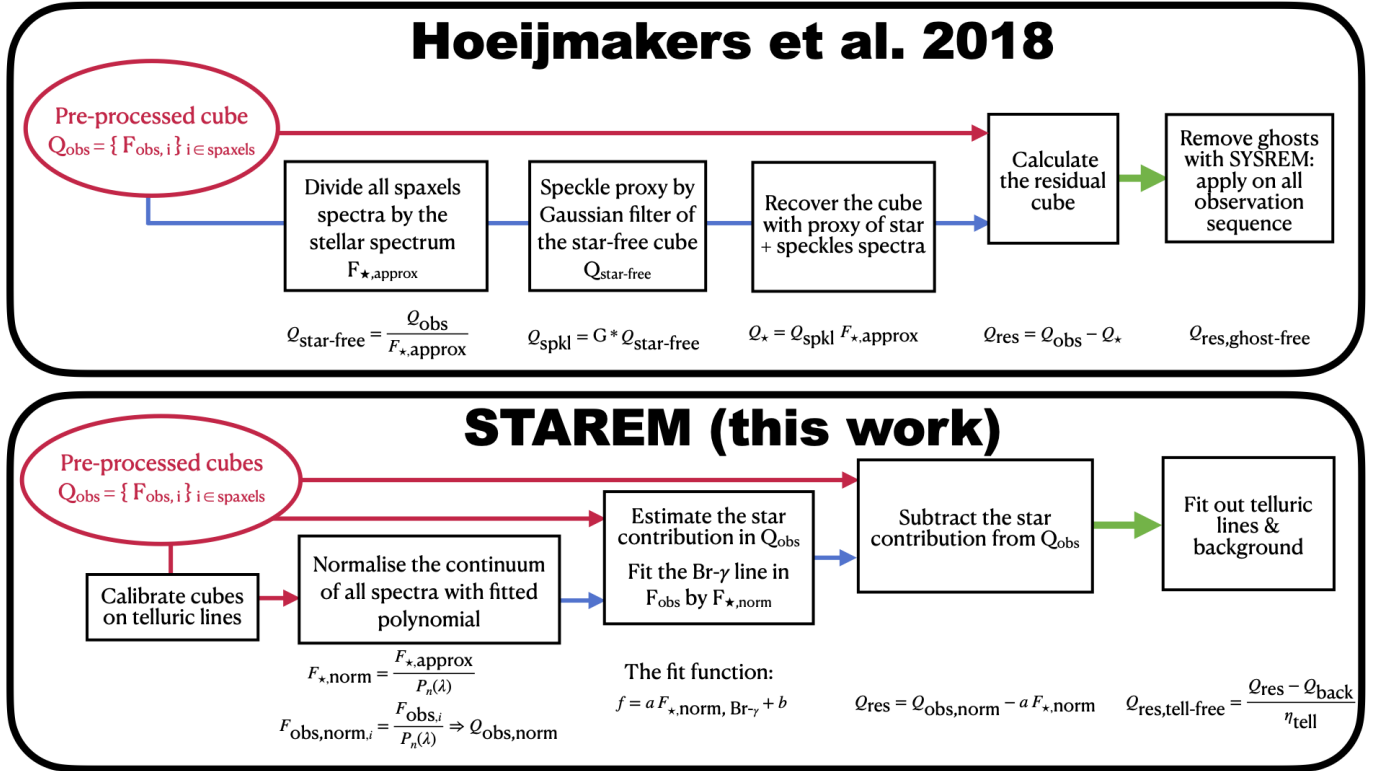


**Fig. 5.** Steps of star spectrum removal methods compared.  $Q_{\text{Obs}}$  stands for the stacked cube observed, while  $\{Q_{\text{Obs}}^{(i)}\}$  refer to the full series of cubes collected during the night.

### 2.5. Science cubes stacking

We aligned the 24 science cubes taken on the 17th of November upon the star centroid. Then, the cubes were de-rotated in such a way that the planet halo is brought at the same  $(\alpha^*, \delta)$ -coordinates in every cube and at every wavelength. We use the values obtained with TExTRIS as explained in Sect. 2.2. This includes a 2D linear interpolation using the `interpolate.griddata` routine from `scipy` in order for all the shifted-rotated cubes to share a common  $(\alpha^*, \delta)$ -grid. Then the 24 cubes are stacked together using a simple average. No clipping of flux is applied during this process in order to maximise the signal-to-noise ratio (S/N). This gives us the data cube that we use in the rest of the analysis; we name it the ‘master cube’ and it is denoted  $Q_{\text{Obs}}$ .

## 3. Star spectrum removal with STAREM

### 3.1. A summary of H18 method

The H18 method used to remove the stellar halo proved to work well for performing molecular mapping of exoplanets. However, it does not allow for the extraction of a pure planet atmosphere transmission spectrum where systematic deviations remain. We will summarise the H18 method here to show where is the identified issue. A sketch of the different steps of this method is shown in Fig. 5. The components of the flux at the planet spaxels,  $i_p$ , are as follows:

$$F_{i_p}(\lambda) = F_{i_p, \star}(\lambda) + F_{i_p, \text{p}}(\lambda) + F_{i_p, \text{B}}(\lambda). \quad (1)$$

Among these parameters, the star flux,  $F_{i_p, \star}$ , and the planet flux,  $F_{i_p, \text{p}}$ , as well as a possible background component,  $F_{i_p, \text{B}}$  (setting the latter aside at present for the simplicity, we note that

it can be added everywhere by duplicating the planet components and changing ‘p’ with ‘B’ in the index; see discussion in Sect. 3.3). We also dropped the ‘ $i_p$ ’ index in the following to alleviate the equations.

The planet and star spectra are each composed of a continuum (hereafter denoted  $C$ ) multiplied by a ‘flat’ transmission spectrum, whose continuum is normalised to 1 everywhere (hereafter denoted  $\eta$ ). Both the astrophysical source and telluric lines contribute to this transmission spectrum. This can also be expressed as  $\eta = 1 - A$ , with  $A$  as a positive comb of spectral lines with the continuum equal to zero everywhere. We point out that the  $A_{\star}$  and  $A_p$  values for the star and the planet, respectively, are supposed to be spaxel-independent, since they are intrinsic to the respective sources. The continua  $C_p$  and  $C_{\star}$  are on the other hand spaxel-dependent because of the PSF and the wavelength-dependent speckles.

In H18, to remove the star and single-out the planet, an approximated star spectrum  $F_{i, \star, \text{approx}}$  that accounts for wavelength-dependent spaxel-to-spaxel variations was subtracted from each spaxel,  $i$ , of the cube,  $Q_{\text{Obs}}$ . They divided each spaxel spectrum by the star spectrum determined (as explained in Sect. 2.3) by averaging some of the brightest spaxels of the master cube. The ‘star-free’ cube  $Q_{\text{star-free}}$  thus obtained displays low-frequency wavelength-dependent variations that differ in the spectra from one spaxel to the other. They are due to speckle patterns over the detector changing with wavelength. Those speckle patterns are modeled by applying a Gaussian filter,  $G$ , on this star-free spectrum,  $G * Q_{\text{star-free}}$ . It results in a speckle-proxy cube, denoted  $Q_{\text{spkl}}$  in Fig. 5. By multiplying those modelled variations by the star spectrum, they finally obtained the star cube  $Q_{\star}$ , with a star spectrum,  $F_{i, \star, \text{approx}}$ , at each spaxel,  $i$ , which accounts for wavelength-dependent spaxel-to-spaxel variations.

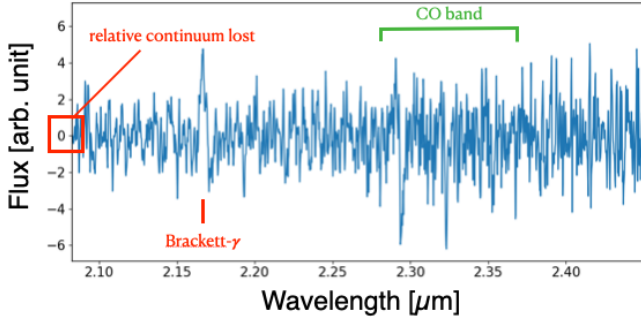


**Fig. 6.** Raw  $\beta$  Pic b spectrum extracted from the planet spaxels after using H18 method of star light removal. SYSREM was not used here. We highlight in red the main artefact that is due to excess star spectrum lines removal at the Brackett- $\gamma$  wavelength. We also note that since the continuum has been subtracted, the reference level to which compare the strength of planet molecular lines (CO shown in green) is missing.

At any spaxel other than the planet spaxels, subtracting  $F_{i,\star,\text{approx}}$  removes the contribution of the star spectrum. However, at the planet spaxel, this is not valid. Indeed, the approximated star spectrum contains contributions from both the star and the planet continuum:

$$F_{\star,\text{approx}} = (C_p(\lambda) + C_{\star}(\lambda))\eta_{\star}(\lambda). \quad (2)$$

By slightly overestimating the star contribution, the subtraction of  $F_{\star,\text{approx}}$  instead leads to:

$$\Delta F(\lambda) = C_p(\lambda)(A_{\star}(\lambda) - A_p(\lambda)). \quad (3)$$

A supplementary stellar contribution (including tellurics) to the residual absorption spectrum remains seen as emission lines, with amplitudes comparable to the planet absorption lines. This is shown in Fig. 6. We note that the persistence of polluting  $\text{CH}_4$  lines led H18 to apply several runs of SYSREM (Tamuz et al. 2005) to remove them. However, this operation does not fix the above issue and the stellar lines still remain in the spectrum at the planet spaxels.

The presence of the star spectrum with a non-negligible amplitude is problematic. Moreover, since the continuum has been subtracted, there is no longer any reference level to which we can compare the strength of molecular lines in the resulting spectrum. As long as the CCF of the star spectrum and the spectra of any of the species found in exoplanet atmosphere is close to zero, this works well for molecular mapping. This is the case here with a 8000 K star and a <2000 K planet. Nonetheless,  $\Delta F$  is not strictly-speaking a pure planet atmosphere spectrum. This issue might also explain the detection of an Br- $\gamma$  emission line in the PDS-70 b spectrum derived with the same H18 method in Cugno et al. (2021). Thus, we suspect it is an artefact from the stellar spectrum removal.

### 3.2. STAREM: A new STAR spectrum REMoval method

We propose a different method to subtract the star spectrum, which we named STAREM and which instead makes use of the normalised transmission spectrum,  $\eta = F/C$ . In this spectrum, we aim to estimate the contribution of the star in any spaxel spectrum,  $F_i$ , by fitting the stellar absorption lines and then subtracted it from  $F_i$ . We demonstrate that this can lead to a well defined flattened transmission spectrum of the planet atmosphere, where the star spectrum is fully removed and the line strength is preserved.

First of all, we normalise all spectra of the observed cube, as well as the star spectrum, by fitting a sixth-degree polynomial to their continuum, leading to a normalised star spectrum of  $F_{\star,\text{norm}}$  and a normalised cube of  $Q_{\text{obs,norm}}$ . Recalling Eq. (1), the normalised transmission spectrum components of  $F = C\eta$  at one of the planet spaxels in  $Q_{\text{obs}}$  are:

$$\eta(\lambda) = \frac{C_{\star}(\lambda)\eta_{\star}(\lambda) + C_p(\lambda)\eta_p(\lambda)}{C(\lambda)}. \quad (4)$$

We recall that the star and planet pseudo-continua are fixed by the star and planet intrinsic pseudo-continua multiplied by the Strehl ratio and PSF (including speckles) damping of the flux. We introduce the star and planet contribution levels,  $K_{\star}$  and  $K_p$ , as:

$$K_{\star}(\lambda) = 1 - K_p(\lambda), \quad (5)$$

$$K_p(\lambda) = \frac{C_p(\lambda)}{C(\lambda)}.$$

The transmission spectrum  $\eta(\lambda)$  can be expressed more compactly as:

$$\eta(\lambda) = K_{\star}(\lambda)\eta_{\star}(\lambda) + K_p(\lambda)\eta_p(\lambda). \quad (6)$$

If we wish to subtract the star contribution,  $K_{\star}\eta_{\star}$ , from this spectrum, we need to estimate  $K_{\star}(\lambda)$ . This can be achieved by comparing the amplitude of the stellar lines to those of a reference stellar spectrum without contributions from the planet; here, a ratio of 1 implies a pure stellar spectrum, namely,  $K_{\star}=1$ . Ideally, with several stellar lines present all through the observed band, the best approach would be to use all the lines so as to obtain a more reliable wavelength-dependent approximation of the  $K_{\star}(\lambda)$  function. In the specific case of the K-band spectrum of  $\beta$  Pic, since the Brackett- $\gamma$  line at 2.165  $\mu\text{m}$  is the only strong feature in this spectral band, we were only able to derive an approximated constant star contribution  $\sim K_{\star}(\lambda_0=2.165 \mu\text{m})$ ; also noted as  $K_{\star,2.165}$  hereafter. The derived values of  $K_{\star,2.165}$  and its pendent residual contribution,  $1 - K_{\star}$ , through the SINFONI field-of-view around  $\beta$  Pic b, are shown in Fig. 7.

Removing an approximated contribution,  $K_{\star,2.165}\eta_{\star}$ , at each spaxel of  $Q_{\text{obs,norm}}$  leads to a residual cube  $Q_{\text{res}}$ . In this cube, the residual spectrum obtained on a planet spaxel is:

$$\eta_{\text{res}}(\lambda) = (K_{\star}(\lambda) - K_{\star,2.165})\eta_{\star}(\lambda) + K_p(\lambda)\eta_p(\lambda). \quad (7)$$

Using Eq. (5), this could equivalently be written as:

$$\eta_{\text{res}}(\lambda) = (K_{p,2.165} - K_p(\lambda))\eta_{\star}(\lambda) + K_p(\lambda)\eta_p(\lambda). \quad (8)$$

This is a flat spectrum whose baseline level is  $K_{p,2.165} = 1 - K_{\star,2.165}$ . At the planet spaxels, it should contain the normalised spectrum of the planet with an amplitude corresponding to the relative flux of the planet compared to the star at 2.165  $\mu\text{m}$ . Because of the normalisation of the planet spectra by the continuum of the star, this is only an approximation. Indeed, away from Brackett- $\gamma$  (more generally from any fitted stellar line) the line amplitudes are impacted by a residual star spectrum component with an amplitude of  $\delta K(\lambda) = K_{p,2.165} - K_p(\lambda)$ . This is a footprint of the planet and the star continua within the flat spectrum. Unfortunately, we cannot assume that  $\delta K\eta_{\star} \approx 0$  because it generates a warp of the planet spectrum lines deviating from one to a few tens of percent, as shown in Fig. 8. This will have to be taken into account later on when analysing the spectrum extracted from the planet spaxels.

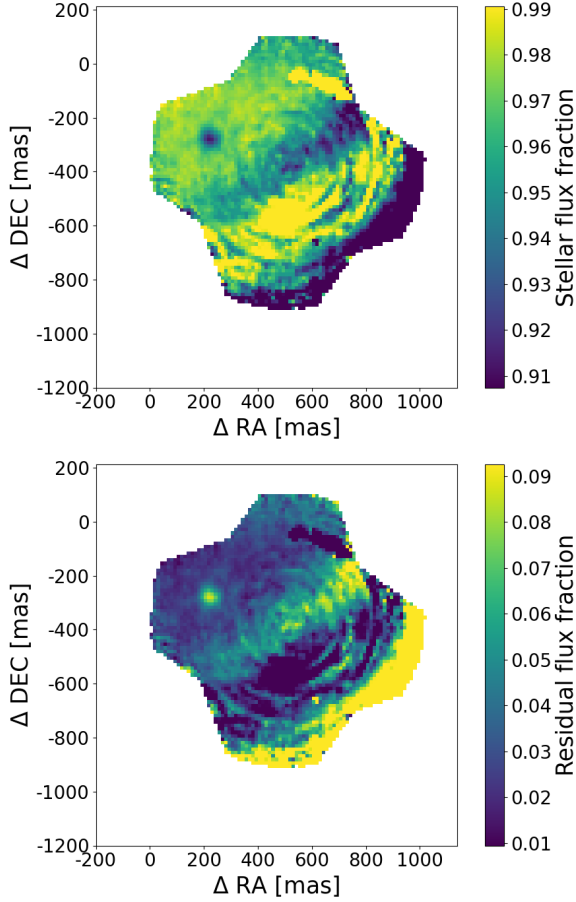


**Fig. 7.** Star flux fraction,  $K_{i,*}$  at  $\lambda=2.165 \mu\text{m}$  (top panel). The corresponding planet flux fraction,  $1 - K_{i,*}$ , at the same wavelength (bottom panel). It can be seen that some background components contribute to the residuals.

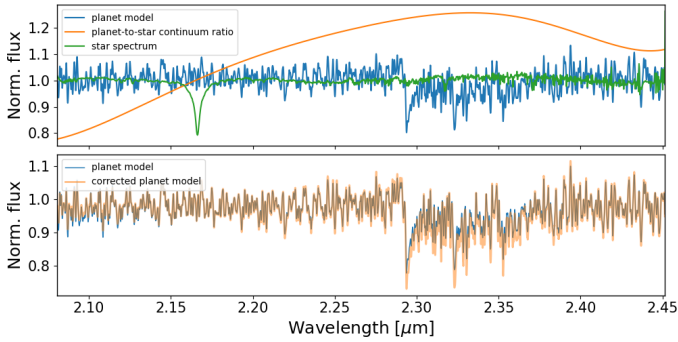


**Fig. 8.** Warp function  $\delta K(\lambda)$  (orange) normalised to 1 at the Brackett- $\gamma$  wavelength (top panel), compared to a normalised Exo-REM model with  $T=1750 \text{ K}$ ,  $\log g = 4.0$ ,  $[\text{Fe}/\text{H}]=0.0$ , and  $\text{C}/\text{O}=0.55$  (blue) as well as the normalised stellar spectrum  $\eta_{i,*}$  (green) of  $\beta \text{ Pic}$  on the  $K$ -band. Residual telluric absorptions can be seen in the stellar spectrum. Naked Exo-REM model (blue) compared to the warped model (orange) is given in the bottom panel.

### 3.3. Tellurics and background removal

In Sect. 2.4, we describe how the tellurics were fitted directly in each of the 24 cubes to the normalised reference star spectrum obtained from the brightest spaxels. They were only used for purpose of calibration. We did not wish to remove tellurics at the next step because removal might introduce residuals with

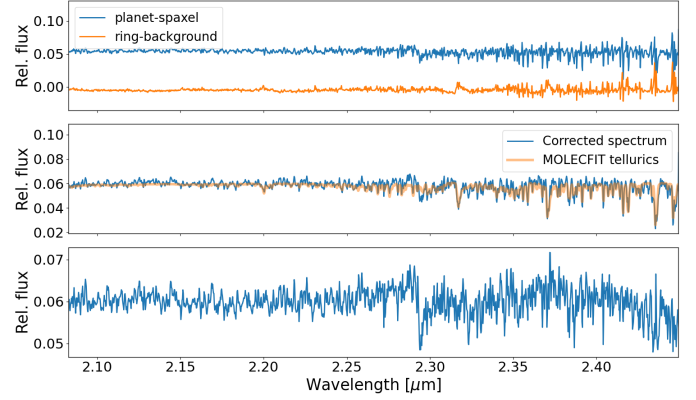


**Fig. 9.** Background-subtraction and telluric removal from a planet-spaxel spectrum. Top: planet spaxel spectrum and average background on a distant ring. Middle:  $\eta_{\text{res,corr}}$  compared to its fitted telluric model  $\eta_{\text{tell}}$ . Bottom: planet-spaxel spectrum corrected from background and tellurics.

amplitudes on the order of magnitude – or worse, even larger amplitudes than the planet would feature.

With the residual cube,  $Q_{\text{res}}$ , in hand, which mainly features the planet and background, we now wish to remove the many tellurics lines that are still present in the observed spectrum in the  $K$ -band. In a more straightforward way, we could fit a model telluric spectrum to any spaxel spectrum in the cube using `molecfit`. However, it is quite time consuming to run `molecfit` with a cube of about 10 000 spaxels and also given the S/N of the residual spectra is poor. Instead, we preferred to use `molecfit` on the star spectrum derived from the stacked cube at the position of the planet. This allows us to obtain a reliable telluric model,  $\eta_{\text{model}}$ , to correct again the wavelength solution, using the same settings as in Sect. 2.4. In doing so, we determined the effective spectral resolution at the position of the planet in the stacked cube to be  $4020 \pm 30$ .

At each spaxel,  $i$ , of the residual cube, we fit out this telluric model,  $\eta_{\text{model}}$ , from  $\eta_{i,\text{res}}$ . To do so, we first needed to correct for a wavelength-dependent background contribution whose non-zero level causes an artificial decrease in the prominence of the telluric lines and the appearance of spurious features, such as telluric lines residuals. These can be seen by comparing a planet-spaxel spectrum and its surrounding background (Fig. 9). The origin of the continuum level of the background is unknown, but it could be due to scattered stray light. The features are generated by the differences between the stellar (plus telluric) spectrum actually observed at the given spaxel and the reference stellar (plus telluric) spectrum (removed in Sect. 2.3<sup>4</sup>).

We make an estimation of the background contribution in a spaxel  $i$  by taking the median spectrum in a distant ring around this spaxel  $\eta_{i,\text{ring}}$ . Since the SINFONI PSF has a FWHM of  $\sim 4$  spaxels in radius, we used a ring radius of six spaxels with a width of one spaxel. This background estimate is then removed from the spaxel,  $i$ , spectrum of  $\eta_{i,\text{res,corr}} = \eta_{i,\text{res}} - \eta_{i,\text{ring}}$ . Its contribution level at  $\sim 2.165 \mu\text{m}$  can be viewed (in Fig. 7) in the brighter areas away from the planet’s location. Figure 1 also shows the  $2.165\text{-}\mu\text{m}$  absolute background flux, which is  $\sim 1\text{--}10\%$  of the absolute total flux at every spaxel. Around the planet

<sup>4</sup> Spaxel-to-spaxel variations in the telluric spectrum arise from small differences in the wavelength calibration from one spaxel to the others, and from adding a non-zero spaxel-dependent background continuum when fitting and subtracting the reference stellar (plus telluric) spectrum in Sect. 3.2.



location, its continuum level is very close to zero, but non-negligible features are seen that have corresponding features in the spectrum at the planet's central spaxel.

Adding a background term to Eq. (8), the background subtraction can be summarised with the following set of equations:

$$\eta_{i,\text{res,corr}} = (K_{i,p,2.165} + K_{i,b,2.165} - K_{i,p} - K_{i,b})\eta_{\star} + K_{i,p}\eta_p + K_{i,b}\eta_b - (K_{\text{ring},b,2.165} - K_{\text{ring},b})\eta_{\star} - K_{\text{ring},b}\eta_b. \quad (9)$$

Assuming an equal contribution of background in the central and the neighboring spaxels, namely,  $K_{i,b} = K_{\text{ring},b}$ , this equation can be simplified to:

$$\eta_{i,\text{res,corr}} = (K_{i,p,2.165} - K_{i,p})\eta_{\star} + K_{i,p}\eta_p. \quad (10)$$

Thus, we are able to recover Eq. (8) and the previously implicit background is now explicitly suppressed. The final step is to fit  $\eta_{\text{model}}$  (the telluric spectrum model) to  $\eta_{i,\text{res,corr}}$ . We use a simple least-squares optimisation at each spaxel, allowing the telluric model to vary in intensity with  $\eta_{i,\text{tell}} = a\eta_{\text{model}} + b$  with  $a + b = c_i$ , if  $c_i$  is the level of the residuals at spaxel  $i$ . Because  $\eta_{\text{model}}$  was determined from the reference stellar spectrum (which could be a slightly affected by the background), an offset ( $b$ ) is added to account for small intensity differences in telluric lines between  $\eta_{\text{model}}$  and the telluric spectrum at a spaxel,  $i$ . We divide  $\eta_{i,\text{tell}}$  from  $\eta_{i,\text{res,corr}}$ , leading to the telluric-free spectrum of  $\eta_{i,\text{res,tell-free}}$ . A summary of the background subtraction and telluric removal at the central planet spaxel is shown in Fig. 9.

## 4. Molecular mapping dedicated to SINFONI spectra

### 4.1. Exo-REM grid of models

To determine the molecular mapping of diverse species in the atmosphere of  $\beta$  Pic b, as is now most commonly performed (see e.g. Snellen et al. 2014; Brogi et al. 2018; Hoeijmakers et al. 2018; Petit dit de la Roche et al. 2018; Ruffio et al. 2019; Cugno et al. 2021; Petrus et al. 2021; Patapis et al. 2022; Mâlin et al. 2023), we calculated a CCF of the observed spectrum at each spaxel with a synthetic spectrum. Here, the templates are taken from an Exo-REM model grid (Baudino et al. 2015; Charnay et al. 2018; Blain et al. 2021). Exo-REM is a 1D radiative-convective model, which self-consistently computes the thermal structure, the atmospheric composition, the cloud distribution and spectra. The model includes the opacities of  $\text{H}_2\text{O}$ ,  $\text{CH}_4$ ,  $\text{CO}$ ,  $\text{CO}_2$ ,  $\text{NH}_3$ ,  $\text{PH}_3$ ,  $\text{TiO}$ ,  $\text{VO}$ ,  $\text{FeH}$ ,  $\text{K}$ , and  $\text{Na}$ , along with the collision-induced absorptions of  $\text{H}_2\text{-H}_2$  and  $\text{H}_2\text{-He}$ . Silicate and iron clouds are included using simple microphysics to determine particle sizes (Charnay et al. 2018). The model grid includes four free parameters totaling 9573 spectra, with  $T_{\text{eq}}$  ranging from 400 to 2000 K with steps of 50 K;  $\log g$  from 3.0 to 5.0 dex with steps of 0.5 dex; and  $[\text{M}/\text{H}]$  from  $-0.5$  to 1.0 dex with steps of 0.5 and  $[\text{C}/\text{O}]$  from 0.1 to 0.8 with steps of 0.05. The synthetic spectra were computed at  $R=20\,000$ , which reflects a compromise between reducing computation speed and reaching the highest resolution possible on atmospheric models to be used as templates of low-to-medium resolution spectra of exoplanets.

We cleansed the model grid from those that did not converge well. To do so, for each spectrum, we calculated the integral on the whole wavelength domain from visible to far IR,  $I_s$ . We compared this integral to the theoretical  $\sigma T_{\text{eff}}^4$  Stefan-Boltzman law.

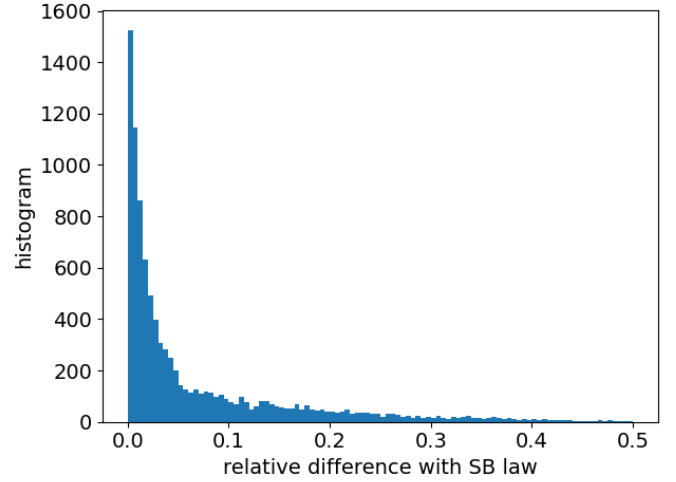


**Fig. 10.** Histogram of relative difference between the exo-REM models emittance and Stefan-Boltzman law.

This deviation peaks below  $\sim 5\%$  (Fig. 10). We thus removed 3315 among 9573 spectra (i.e. 35%) with a deviation larger than 5%.

Each synthetic spectrum produced by Exo-REM results from individual contributions (or spectrum) of the species out of which it is composed, mainly  $\text{CO}$ ,  $\text{H}_2\text{O}$ ,  $\text{CH}_4$ , and  $\text{NH}_3$ , which we can use as individual molecular templates.

### 4.2. The cross-correlation function of the planet spectrum

At every spaxel, between 2.08 and 2.43  $\mu\text{m}$ , we calculate the CCF of the observed spectrum and an Exo-REM synthetic spectrum for an assumed  $T_{\text{eff}}=1700$  K,  $\log g=4.0$  cgs, and  $[\text{Fe}/\text{H}]=0.0$  dex, as based on Table 3 in GRAVITY Collaboration (2020). The expected abundances of  $\text{NH}_3$  and  $\text{CH}_4$  in the atmosphere  $\sim 10^{-6}$  are too low to yield absorption features detectable in the SINFONI spectra. Thus, we artificially enhanced their abundances to  $10^{-4}$ , in order to probe possible over-abundance of these species in  $\beta$  Pic b's atmosphere. Details on the contributions of  $\text{H}_2\text{O}$ ,  $\text{CO}$ ,  $\text{NH}_3$  and  $\text{CH}_4$  are shown in Fig. 11 and compared to the  $\beta$  Pic b's spectrum derived in next Sect. 5.

We excluded the red edge of the  $K$ -band beyond 2.43  $\mu\text{m}$ , which displays the strongest telluric lines remnants. Prior to the calculation, we divided the continuum of the observed and synthetic spectra. The continuum is obtained by first fitting a fourth-degree polynomial and then applying a median filter with a window-width of 0.01  $\text{\AA}$ , combined to a smoothing Savitzky-Golay filter of order 1. The CCF is calculated by directly cross-correlating the median-removed observed and synthetic spectra at different shifts. The CCF is finally normalised by the norm of the spectra, thus leading to a zero-normalised CCF. This results in the molecular maps shown in Fig. 12.

We then fit the PSF of the planet CCF halo by a 3D Gaussian with respect to  $(\delta, \alpha, v_r)$ . This determines the position and radial velocity of the planet, as well as the broadening of the PSF and of the LSF. The results are summarised in Table 1. They are compared to the values derived in the same fashion but following H18's recipe to suppress the stellar pollution. We only show the results for  $\text{CO}$ ,  $\text{H}_2\text{O}$ , and (using the full spectrum, confirming, as in H18) the presence of  $\text{CO}$  and  $\text{H}_2\text{O}$ , but not detecting  $\text{NH}_3$  and  $\text{CH}_4$ . With some variability from one model to the other, the CCF peak is located at a separation to the central

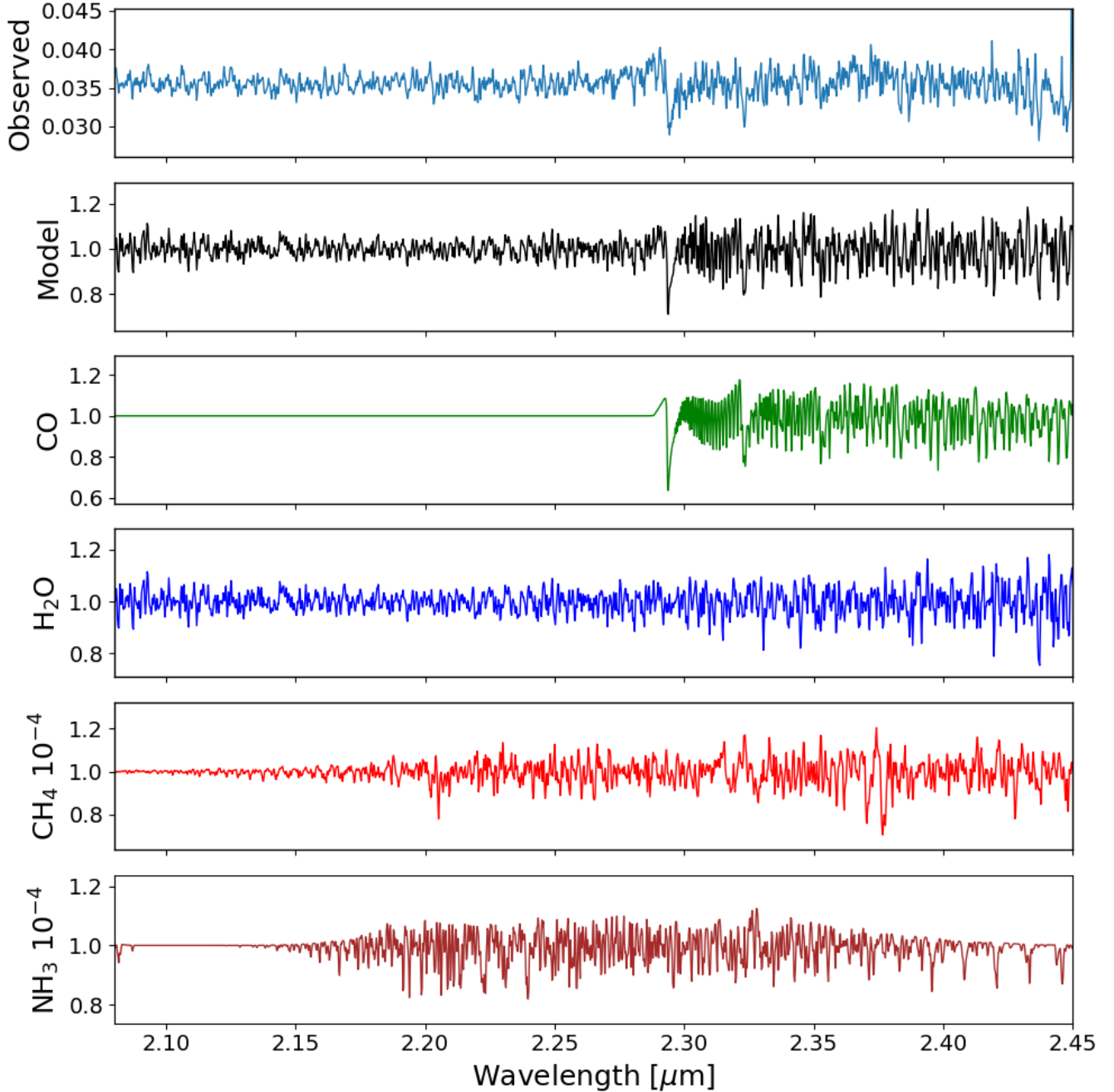


**Fig. 11.** SINFONI planet absorption spectrum of  $\beta$  Pic b along the  $K$ -band, once corrected from star, background, and telluric pollutions (top). Exo-REM spectrum of simulated atmosphere of 1700 K,  $\log(g)=4.0$ , and  $[\text{Fe}/\text{H}]=0.0$  with  $R=6000$  (bottom). Individual contributions of species CO,  $\text{H}_2\text{O}$ ,  $\text{CH}_4$ , and  $\text{NH}_3$  are represented from top to bottom with diverse colors. For all the spectra, their continuum were divided, as explained in Sect. 4.2.

star of  $\sim 351 \pm 5$  mas, with a PSF broadening standard deviation of  $\sim 2.7$  spaxels, that is 34 mas.

The S/N is calculated as the height of the peak divided by the fit residuals on a volume of  $200 \text{ pix}^2$  by  $2000 \text{ km s}^{-1}$  around the planet ( $\delta, \alpha, v_r$ )-location. Our `starem` method leads to S/N values that are comparable to those obtained through H18 method. We did not use `SYSREM` as they did to remove the spaxel-to-spaxel correlated noise within the cubes, but corrected for the background differently (as explained in Sect. 3.3). We derived a slightly better S/N by subtracting the star halo using `STAREM` (instead of those obtained using the H18 subtraction method), leading to  $S/N_{\text{all}}=19.6$ ,  $S/N_{\text{CO}}=11.8$ , and  $S/N_{\text{H}_2\text{O}}=15.4$ . This also

follows the trend found for HIP 65426 b (Petruš et al. 2021), whereby taking into account all species leads to the best detection S/N; while for individual contributions of species,  $\text{H}_2\text{O}$  gives significantly better results than CO. These last properties is best explained by the presence of less prominent but more numerous lines of  $\text{H}_2\text{O}$  compared to CO all along the  $K$ -band and, especially, away from regions spanned by telluric lines.

We note that in H18 paper, the S/N values they obtained are greater (all molecules: 22.8 vs. 17.5 here; CO: 13.7 vs. 11.2 here;  $\text{H}_2\text{O}$ : 16.4 vs. 15.7 here). This difference can be explained by the fact that they averaged the CCF of cubes obtained at two different nights, while we used the cubes from only a single night. The

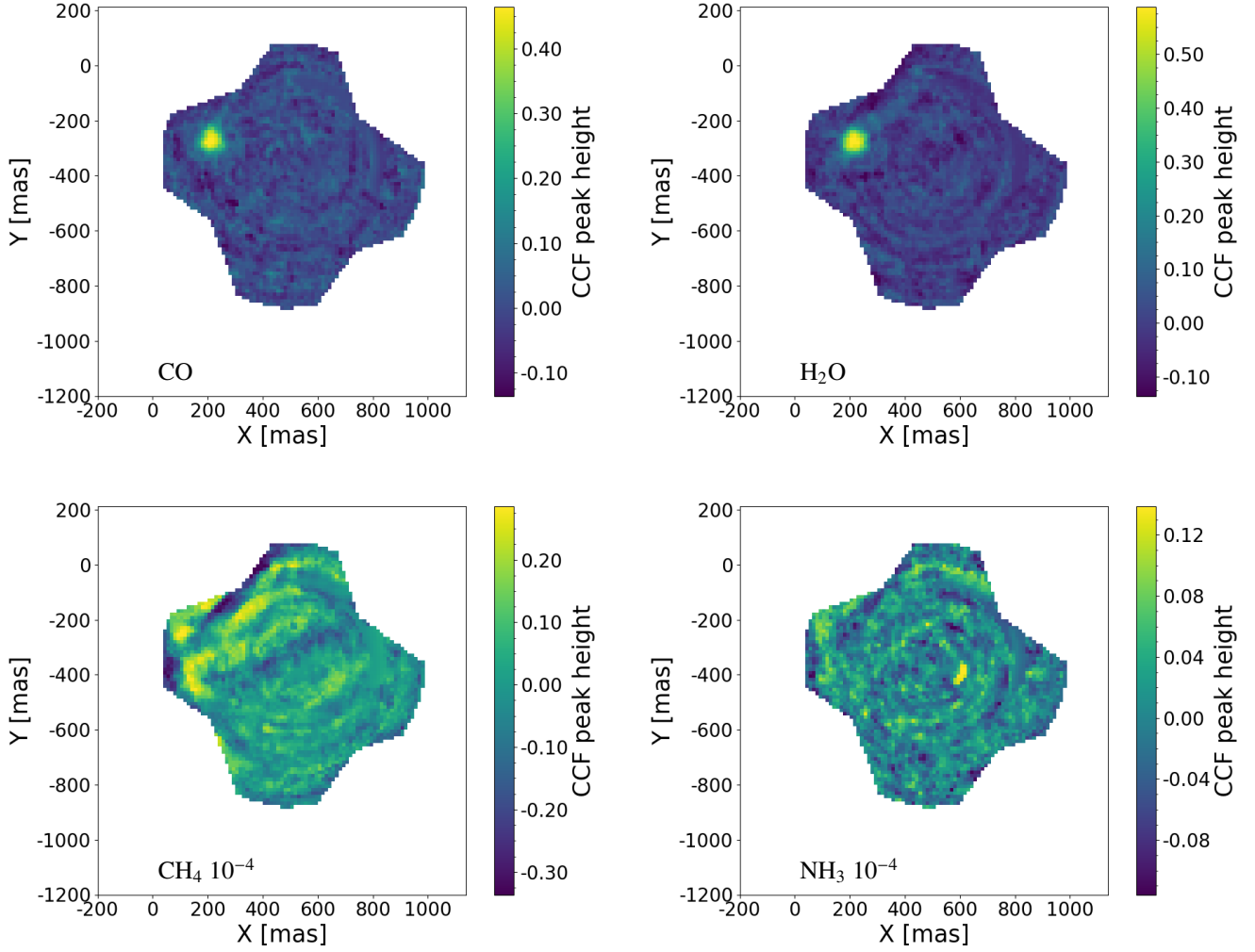


**Fig. 12.** Molecular CCF maps of  $\beta$  Pic b for species CO, H<sub>2</sub>O, CH<sub>4</sub> ( $10^{-4}$ ) and NH<sub>3</sub> ( $10^{-4}$ ). At each spaxel, the maps show the CCF height at  $0 \text{ km s}^{-1}$ , a value close to the expected radial velocity of the planet  $b$ ,  $|VR| < 10 \text{ km s}^{-1}$  given the instrument LSF of  $\sim 75 \text{ km s}^{-1}$ .

**Table 1.** Comparing results of the different star spectrum subtraction schemes on the normalised CCF of the residual map with a  $1700 \text{ K}$ ,  $\log g=4.0$ ,  $[\text{Fe}/\text{H}]=0.0$  Exo-REM model, detailing the CO and H<sub>2</sub>O individual contributions.

Method	CCF strength			Radial velocity		$X_c$ ( $\dagger$ ) (mas)	Planet PSF	
	Peak height	noise level	S/N	$v_r$ ( $\text{km s}^{-1}$ )	$\sigma_{\text{broad}}$ ( $\text{km s}^{-1}$ )		$Y_c$ ( $\dagger$ ) (mas)	$\sigma_{\text{PSF}}$ (pixel)
Full-model: $1700 \text{ K}$ , $\log g=4.0$ , $[\text{Fe}/\text{H}]=0.0$ , $R_{\text{spec}}=6000$								
H18	$0.8952 \pm 0.0076$	0.0511	$17.52 \pm 0.15$	$1.03 \pm 0.35$	$46.80 \pm 0.38$	$218.0 \pm 0.25$	$-277.13 \pm 0.25$	$2.34 \pm 0.01$
STAREM	$0.8452 \pm 0.0060$	0.0431	$19.60 \pm 0.14$	$-0.25 \pm 0.25$	$41.87 \pm 0.30$	$216.63 \pm 0.25$	$-276.75 \pm 0.25$	$2.71 \pm 0.01$
Only CO								
H18	$0.4837 \pm 0.0049$	0.0432	$11.20 \pm 0.11$	$-4.29 \pm 0.41$	$45.91 \pm 0.49$	$215.38 \pm 0.25$	$-274.25 \pm 0.25$	$2.47 \pm 0.02$
STAREM	$0.5094 \pm 0.0048$	0.0431	$11.81 \pm 0.11$	$-3.24 \pm 0.35$	$41.85 \pm 0.42$	$214.00 \pm 0.25$	$-273.50 \pm 0.25$	$2.66 \pm 0.02$
Only H <sub>2</sub> O								
H18	$0.7887 \pm 0.0076$	0.0523	$15.07 \pm 0.15$	$2.28 \pm 0.38$	$41.64 \pm 0.33$	$218.62 \pm 0.25$	$-278.63 \pm 0.25$	$2.28 \pm 0.02$
STAREM	$0.6947 \pm 0.0056$	0.0451	$15.41 \pm 0.12$	$0.76 \pm 0.29$	$41.64 \pm 0.33$	$217.13 \pm 0.25$	$-279.00 \pm 0.25$	$2.75 \pm 0.02$

**Notes.** We also tried the molecular mapping on CH<sub>4</sub>, NH<sub>3</sub>, FeH, and CO<sub>2</sub>, none leading to a significant detection within the area around planet spaxels. ( $\dagger$ )The star is located at coords  $(X_*, Y_*)=(0,0)$  mas.

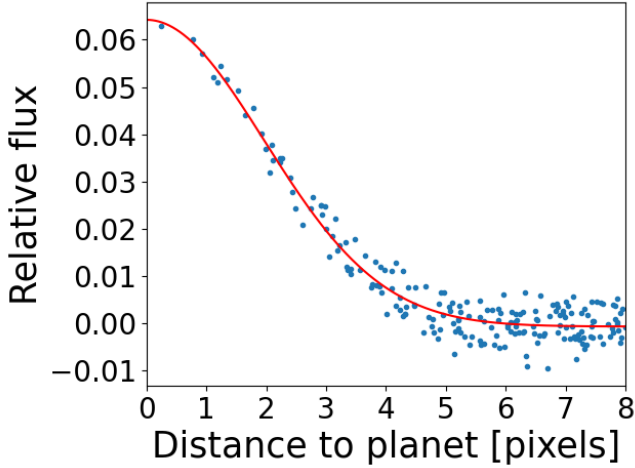


**Fig. 13.** Planet PSF radial profile at a varying distance from 0 to 8 spaxels. The relative flux is obtained by dividing out the continuum and subtracting the star spectrum, as explained in Sect. 3.2.

smaller difference of S/N for H<sub>2</sub>O can be explained by the presence of traces of telluric lines in the H18 residual cube because they did not recalibrate the wavelength solution before subtracting the reference spectrum (containing the tellurics). We also note that the calculation performed in H18's paper to determine the S/N is slightly different in that they use a distant 3D-ring around the CCF peak to estimate the noise, while we calculate the noise from the residuals of a fit of the CCF peak.

## 5. Extracting the planet atmosphere absorption spectrum

The PSF of the planet follows an Airy profile whose central region can be approximated by a Gaussian profile. This can be seen in Fig. 13 where the residual flux of the stellar subtraction at 2.165  $\mu\text{m}$  is shown with respect to the distance of the spaxels to the planet centre position. The planet centre position is obtained by fitting the residual flux at 2.165  $\mu\text{m}$  by a 2D Gaussian. The radial profile of the planet PSF is well modeled by a two-spaxel wide Gaussian. The planet relative flux rises up to 7% near the centre, but becomes negligible compared to noise beyond a distance of about five spaxels.

The average spectrum at those spaxels is calculated by integrating the relative flux on all spaxels up to a given radius and applying to each spaxel a weight that depends on its distance to the planet. We model the PSF profile by the Gaussian used above, with  $F(r)=e^{-r^2/2\sigma_{\text{PSF}}^2}$  and where  $r=||\mathbf{r}_i - \mathbf{r}_c||$  is the spaxel-distance between a given spaxel,  $i$ , and the planet centre position, and  $\sigma_{\text{PSF}}=2$  spaxels at 2.165  $\mu\text{m}$ . We used this profile as the weight function with thus  $w(r)=e^{-r^2/2\sigma_{\text{PSF}}^2}$ . When integrating the spaxels flux, both planet and noise signals grow, yet they are still limited by the PSF flux dimming, and the S/N increases as  $\sqrt{N_{\text{spaxels}}}$ . We found it reasonable to integrate the flux up to  $4\text{-}\sigma$  from the PSF centroid, with  $\sigma(\lambda)=\sigma_{\text{PSF}} \times 2.165 \mu\text{m}/\lambda$ .

Since we cannot assume that the background removal was absolutely perfect in Sect. 3.3, we again estimate the background pollution within planet spaxels using neighboring spaxels in a ring around the planet. The background level at distance to the planet centroid is close to zero within  $\pm 0.01$ , as can be seen in the PSF profile (Fig. 13). We use the median spectrum within this ring as an estimation of the background spectrum shown in the top panel of Fig. 14. This background spectrum is subtracted

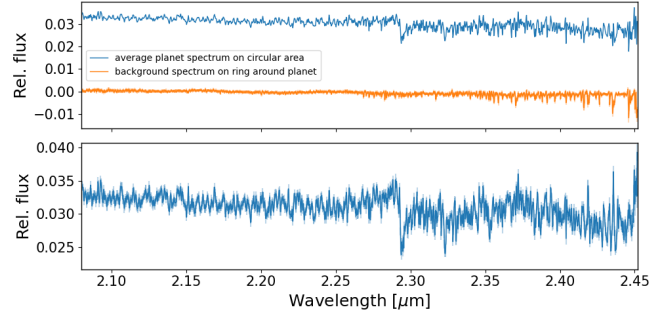


**Fig. 14.** Background removal. Top panel: average spectrum about the planet centroid (blue) compared to the average background spectrum on a ring around the planet (orange). Common features can be well distinguished. Bottom panel: planet spectrum corrected from the background. The features remaining are  $\beta$  Pic b's atmosphere absorption lines, while the main stellar feature (Brackett- $\gamma$ ) has been fully removed.

from the average planet spectrum, leading to the corrected planetary spectrum, also shown Fig. 14. We found the ring radii optimising the S/N of the corrected planet spectrum to be 4.2–5.1 spaxels.

As a final step, the spectrum was divided by the continuum and estimated (as in Sect. 4.2) by applying a median filter with a window-width of 0.01  $\text{\AA}$  combined to a smoothing Savitzky-Golay filter of the order of 1. The final planet spectrum obtained is compared to a theoretical Exo-REM spectrum of a 1700 K planet, with  $\log g=4.0$  cgs and  $[\text{Fe}/\text{H}]=0.0$  dex in Fig. 11.

## 6. Template-matching of the planet spectrum

We addressed the problem of finding the best matching model of the planet spectrum in two ways: first, by exploring the space of available templates and their match with the planet spectrum, using a simple grid search, and, second by running a Markov chain Monte Carlo (MCMC) sampling around the optimum spectrum. In both cases, we used the forward-modeled Exo-REM (Charnay et al. 2018) spectra models of exoplanet atmosphere.

### 6.1. Grid search

We first explored the template space by a grid search. We tested the  $\chi^2$  and zero-normalised CCF scores for optimising the models. Each model spectrum is convolved by a Gaussian Kernel corresponding to a resolving power of 4020 and by a rotational profile with  $v \sin i=25 \text{ km s}^{-1}$ . The rotational profile is the usual bell-like profile with limb-darkening coefficient  $\varepsilon=0.6$  (Gray 1997). Each model spectrum is then flattened with the same median filtering function, with a window width of 0.01  $\mu\text{m}$ , as used to flatten the observed spectrum. Moreover, we corrected for the 'warp' effect (noted in Sect. 3.2) in the models by adding a supplementary term in  $(1 - C_p/C)\eta_*$ , with  $\eta_*$  as the normalised star spectrum,  $C_p$  as the model's continuum, and  $C$  as the average continuum in the SINFONI cube at the planet spaxels, both normalised to 1 at 2.165  $\mu\text{m}$ . For the ZNCCF, the median of both the model and data results is subtracted before the cross-correlation is done. For  $\chi^2$ , the fit function includes two other parameters applied to the model spectrum of a scale,  $a$ , to allow us to compensate for the arbitrary level of the spectrum continuum, and a rigid Doppler shift,  $v_r$ . The fit is then performed using the `curve_fit` procedure from the `scipy` library.

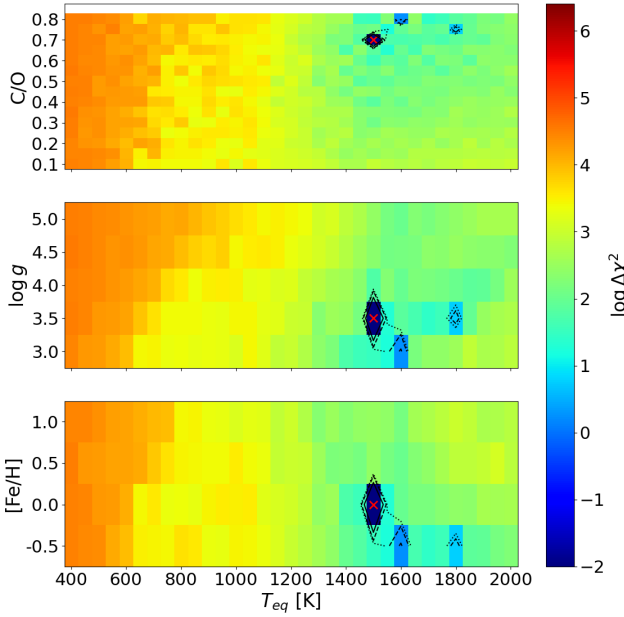


**Fig. 15.** Grid search  $\Delta\chi^2$  maps for  $T_{\text{eff}}-\log g$  (top panel),  $T_{\text{eff}}-C/O$  (middle panel), and  $T_{\text{eff}}-[Fe/H]$ . The solid, dashed, and dotted lines indicate 1, 2, and 3- $\sigma$  confidence regions. The red cross indicates the optimum model.

The error bars of data points are derived from the relation of  $\sigma_{\text{data}} \propto \sqrt{F_{\star, \text{approx}}/C}$ , with  $F_{\star, \text{approx}}(\lambda)$  the reference stellar spectrum defined in Sect. 2.3 and  $C(\lambda)$  the continuum by which spectra are divided in Sect. 3.2. The level of noise is normalised to the error directly measured in the planetary spectrum at  $2.165 \mu\text{m}$  from the standard deviation of flux to the median on a width of  $0.003 \mu\text{m}$ ; we take the average of the errors at all spectral channels from  $2.15$  to  $2.18 \mu\text{m}$ .

The grid search maps with  $\chi^2$ -score and CCF-score are shown, respectively, in Figs. 15 and 16 and the results are summarised in Table 2. For the  $\chi^2$ , the confidence intervals are bounded by the  $\Delta\chi^2$  with the 1, 2, and 3- $\sigma$  regions corresponding to  $\Delta\chi^2=2.3, 6.2,$  and  $11.8$ . For the individual measurements in Table 2, the 1 and 2- $\sigma$  intervals correspond to  $\Delta\chi^2=1$  and 4, interpolated from the 1D  $\Delta\chi^2$  obtained for each parameter. The small extent of the 1- $\sigma$  confidence regions around the best fit model is most likely an effect of the discrete grid used to explore the parameter space. Half the 2- $\sigma$  intervals are certainly more reliable than the 1- $\sigma$  intervals as error bars. For the CCF grid search, we show the  $\Delta\text{CCF}$  regions of 1%, 10%, and 20%; they are not translated into confidence intervals and only the optimum model is given in Table 2.

The  $\chi^2$  grid search leads to a solution with  $T_{\text{eff}}=1550 \text{ K}$ ,  $[Fe/H]=0.0 \text{ dex}$ ,  $\log(g)\sim 3.5$ , and  $C/O\sim 0.70$ . The best matching model is compared to the observed spectrum in Fig. 17. The CCF grid search leads to a different solution with much larger temperature saturating at  $2000 \text{ K}$  and a solar metallicity. However, in this case (as shown in Fig. 17), the spectra do not match in terms of the line amplitude. This shows that the CCF, due to the removal of the continuum and the normalisation of the spectra, is not well adapted to grid search with a strong degeneracy of models.

## 6.2. An MCMC sampling of models

We used emcee (Foreman-Mackey et al. 2013) to apply 1 000 000 iterations of a Markov chain Monte Carlo (MCMC) sampling

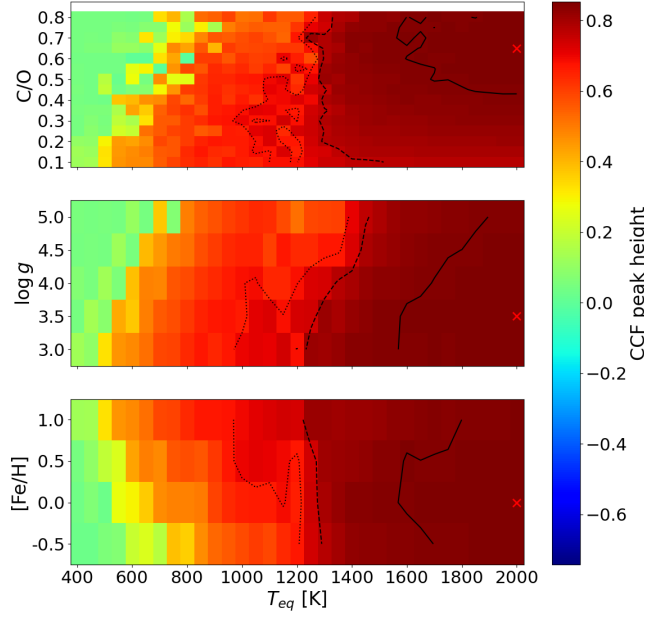


**Fig. 16.** Grid search CCF maps for  $T_{\text{eff}}-\log g$  (top panel),  $T_{\text{eff}}-C/O$  (middle panel), and  $T_{\text{eff}}-[Fe/H]$ . The solid, dashed, and dotted lines indicate 1%, 10%, and 20%  $\Delta\text{CCF}$  levels compared to the optimal CCF. The red cross indicates the optimum model.

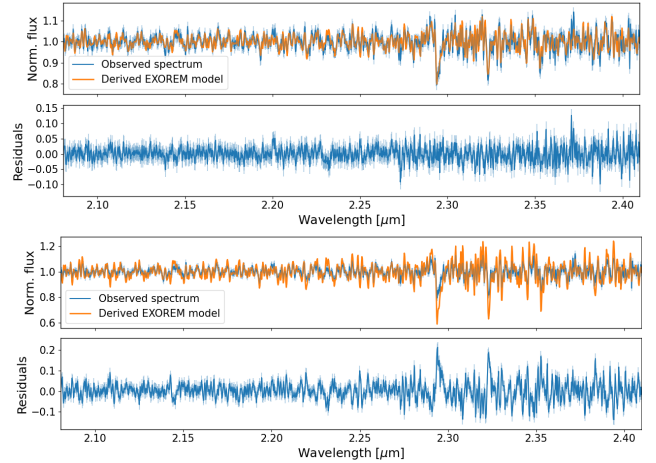


**Fig. 17.** Best-matching models, using the  $\chi^2$  optimisation (top) and the CCF optimisation (bottom).

around the best solution (found by gridsearch in Sect. 6.1) to assess the true posterior distribution and correlations among the varied parameters. The fitted physical parameters are  $T_{\text{eff}}$ ,  $\log g$ ,  $[Fe/H]$ ,  $C/O$ ,  $v_r$ , and  $v \sin i$ . We also fit for the spectral resolving power  $R_{\text{spec}}$ , in order to account for possible deviations from  $R=4020 \pm 30$ . We also sampled a rescaling,  $a$ , to adjust the continuum of model and observed spectra together. The pre-processings of data and models were the same as those used adopted in the gridsearch. The error bars of the data points,  $\sigma_{\text{data}}$ , (as defined in Sect. 6.1) might be over or under estimated by a certain multiplicative amount  $f_{\text{err}}$  and under-estimated by a constant jitter  $\sigma$ . We thus use the error model  $\sigma_{\text{err}}^2 = (f_{\text{err}}\sigma_{\text{data}})^2 + \sigma^2$  with  $\sigma_{\text{data}}$ , depending on wavelength. We added  $f_{\text{err}}$  and  $\sigma$  as hyper-parameters in the MCMC. The prior distributions, either normal  $\mathcal{N}$  or uniform  $\mathcal{U}$ , that we assumed for all parameters are listed in Table 3. All parameters, except  $R_{\text{spec}}$ , follow uniform priors.

**Table 2.**  $\chi^2$  and CCF grid search results (see Sect. 6.1).

Parameter	Unit	$\chi^2$ grid			CCF grid
		Optimum	1- $\sigma$	2- $\sigma$	Optimum
$T_{\text{eff}}$	(K)	1500	(+3)(-1)	(+100)(-5)	2000
$\log g$	(cgs)	3.5	(+0.0)(-0.3)	(+0.0)(-0.5)	3.5
[Fe/H]	(dex)	0.0	(+0.0)(-0.3)	(+0.0)(-0.5)	0.0
C/O		0.70	(+0.01)(-0.00)	(+0.10)(-0.01)	0.65
$^{(\dagger)}v_r$	(km s $^{-1}$ )	0.78	$\pm 0.79$		-1.10
$^{(\dagger)}a$		0.999	$\pm 0.025$		Fixed to 1
$^{(\dagger)}v \sin i$	(km s $^{-1}$ )	Fixed to 25			Fixed to 25
$R$		Fixed to 4020			Fixed to 4020
$\chi_r^2$		1			
max(CCF)					0.69

**Notes.** The reduced optimum  $\chi^2$  has been normalised to 1 and is therefore not given here. Uncertainties are obtained by interpolation of the 1D  $\Delta\chi^2$  maps.  $^{(\dagger)}$ The 1- $\sigma$  error bars for  $v_r$ ,  $v \sin i$ , and  $a$  are obtained for the optimal model using `scipy`'s `curve_fit` procedure. The  $v \sin i$  and  $a$  are not optimised for the CCF, assuming  $v \sin i=25$  km s $^{-1}$  and  $a=1$ .

**Table 3.** Prior probability density functions (PDF) and parameters used for the MCMC runs.

Parameter	Prior PDFs or values
$T_{\text{eff}}$	$\mathcal{U}(400; 2000)$ or $\mathcal{N}(1724; 15)$
$\log g$	$\mathcal{U}(3.0; 5.0)$ or $\mathcal{N}(4.18; 0.01)$
[Fe/H]	$\mathcal{U}(-0.5; 1.0)$
C/O	$\mathcal{U}(0.1; 0.8)$
$v \sin i$	$\mathcal{U}(0, +\infty)$
$R_{\text{spec}}$	$\mathcal{N}(4020; 30)$
$v_r$	$\mathcal{U}(-\infty, +\infty)$
$f_{\text{err}}$	$\mathcal{U}(0.1, 10)$
$\sigma$	$\mathcal{U}(0, 0.5)$
$a$	$\mathcal{U}(0.5, 1.5)$
$N_{\text{steps, max}}$	1 000 000
$N_{\text{walkers}}$	20

**Notes.** For  $T_{\text{eff}}$ , two types of priors are used, which are either uniform along the range of possible values. The MCMC run stops whenever the maximum autocorrelation length among all parameters,  $\max(\tau_i)$ , is larger than 50 times the actual number of iterations.

The Exo-REM model spectra are interpolated through the initial 4D grid at the specific values of parameters chosen by the MCMC walkers at each new step. For a quick calculation, we applied the `LinearNDInterpolator` from `scipy` on the smallest Hull simplex, where each vertex is a model of the Exo-REM grid, surrounding each MCMC sampled point. This accounts for missing models at several grid nodes (see Sect. 4.1 above).

The MCMC runs for (at most) 1 000 000 steps with 20 walkers. It stops whenever the number of steps is smaller than 50 $\times$  the largest auto-correlation length of the samples. Table 4 summarises the results of two different runs, one with all parameters freely varying within uninformed priors (except for  $R$ ). The corner plot shows the posterior distributions with all parameters freely varying in Fig. A.1. The synthetic spectrum at the median of these posterior distributions is compared to the observed data on Fig. A.2. The derived parameters are in good agreement with the initial guess from the grid-search in Sect. 6.1 and lead to more reliable confidence regions, with an effective

temperature ranging at 1- $\sigma$  within  $1555_{-22}^{+29}$  K,  $\log g=3.12_{-0.09}^{+0.12}$ , Fe/H= $-0.325_{-0.045}^{+0.065}$  dex, a super-solar C/O  $\sim 0.79_{-0.11}^{+0.01}$ , and a  $v \sin i=31 \pm 5$  km s $^{-1}$ . Our temperature estimate agrees with the GRAVITY Collaboration (2020) results for the GRAVITY + GPI YJH band data fitted with exo-REM models ( $1590 \pm 20$  K). Also, our derived metallicity and  $\log g$  values agree with the fit of the GRAVITY-only spectrum. However, we found a super-solar C/O; whereas those authors they found it to be sub-solar.

The  $\log g \sim 3.1$  result given above, as well as by the GRAVITY collaboration (GRAVITY Collaboration 2020), implies a planet mass close to  $2 M_J$ . It disagrees with the independent dynamical constraints on the mass of the planet, namely, of  $\sim 12 M_J$  (Snellen & Brown 2018; Lagrange et al. 2020; GRAVITY Collaboration 2020). We thus tried to fix the  $\log g$  at a higher value, around 4.18, as suggested by Chilcote et al. (2017) work, defining a Gaussian prior probability distribution for the  $\log g \sim 4.18 \pm 0.01$ . As shown in Table 4, in this case, the MCMC leads to a larger temperature of  $1746_{-3}^{+4}$  K, and a smaller C/O of  $0.551 \pm 0.002$  compatible with a solar value.

We also tried fixing the  $T_{\text{eff}}$  prior to the Chilcote et al. (2017) value of  $1724 \pm 15$  K, along with both  $\log g$  and  $T_{\text{eff}}$ . These trials are also shown in Table 4 and are compatible with the fixed- $\log g$  trial. We calculated the Akaike information criterion  $\text{AIC}=2k - 2 \ln \mathcal{L}$  for all models. The maximum likelihood estimator (MLE) model obtained with the  $T_{\text{eff}}$  fixed minimises the Akaike information criterion (AIC) and is thus preferred over all other models. The large difference in AIC of  $\Delta\text{AIC} \sim 36$  means that the  $T_{\text{eff}}$ -fixed model is  $2.5 \times 10^{-8}$  times more likely than the model with uninformed priors, and  $1.4 \times$  more likely than the model with both  $\log g$  and  $T_{\text{eff}}$  fixed. This preferred solution has a  $T_{\text{eff}}$  of  $1748_{-4}^{+3}$  K, a  $\log g=4.22 \pm 0.03$  (slightly larger than the Chilcote value of 4.18), a sub-solar Fe/H= $-0.235_{-0.015}^{+0.013}$  dex, a solar C/O  $\sim 0.551 \pm 0.002$ , and a  $v \sin i=25_{-6}^{+5}$  km s $^{-1}$ . In all cases, we found a jitter  $\sigma$  that is compatible with zero, with a correcting factor of error bars  $f_{\text{err}} \sim 1_{-0.11}^{+0.05}$  very close to 1. Both imply that our determination of flux error bars  $\sigma_{\text{data}}$  introduced in Sect. 6.1 is reasonable. Figure 19 shows our preferred model compared to the observed planet spectrum and the corner plot of posterior distributions is shown in Fig. 18.

The radial velocity of the planet is found to be around  $0.6 \pm 0.9$  km s $^{-1}$  in the Earth reference frame. With a barycentric

**Table 4.** MCMC results for the run.

Parameter	Unit	All uniform priors		Prior $\log g = 4.18 \pm 0.01$		Prior $T_{\text{eff}} = 1724 \pm 15$ K		Prior $\log g$ and $T_{\text{eff}}$	
		median $\pm \sigma_{68.3\%}$	MLE	median $\pm \sigma_{68.3\%}$	MLE	median $\pm \sigma_{68.3\%}$	MLE	median $\pm \sigma_{68.3\%}$	MLE
$T_{\text{eff}}$	K	1555 <sup>+22</sup> <sub>-29</sub>	1525	1746 <sup>+4</sup> <sub>-3</sub>	1746	1748 <sup>+3</sup> <sub>-4</sub>	1749	1745 <sup>+3</sup> <sub>-2</sub>	1746
$\log g$	cgs	3.12 <sup>+0.12</sup> <sub>-0.09</sub>	3.24	4.185 <sup>+0.010</sup> <sub>-0.010</sub>	4.182	4.216 <sup>+0.027</sup> <sub>-0.031</sub>	4.210	4.183 <sup>+0.010</sup> <sub>-0.010</sub>	4.190
[Fe/H]	dex	-0.325 <sup>+0.065</sup> <sub>-0.045</sub>	-0.246	-0.235 <sup>+0.014</sup> <sub>-0.011</sub>	-0.226	-0.235 <sup>+0.015</sup> <sub>-0.013</sub>	-0.223	-0.237 <sup>+0.013</sup> <sub>-0.010</sub>	-0.233
C/O	–	0.79 <sup>+0.01</sup> <sub>-0.11</sub>	0.68	0.551 <sup>+0.002</sup> <sub>-0.002</sub>	0.550	0.551 <sup>+0.002</sup> <sub>-0.002</sub>	0.550	0.551 <sup>+0.002</sup> <sub>-0.002</sub>	0.550
$v \sin i$	km s <sup>-1</sup>	31.4 <sup>+4.6</sup> <sub>-5.0</sub>	33.0	27.1 <sup>+4.5</sup> <sub>-5.4</sub>	24.9	24.9 <sup>+5.2</sup> <sub>-6.2</sub>	25.4	26.6 <sup>+4.4</sup> <sub>-5.2</sub>	28.6
$R_{\text{spec}}$	–	4018 <sup>+30</sup> <sub>-30</sub>	4042	4019 <sup>+30</sup> <sub>-30</sub>	4024	4018 <sup>+30</sup> <sub>-30</sub>	4032	4019 <sup>+30</sup> <sub>-30</sub>	4020
$v_r$	km s <sup>-1</sup>	0.77 <sup>+1.05</sup> <sub>-0.97</sub>	1.20	0.58 <sup>+0.86</sup> <sub>-0.89</sub>	0.30	0.62 <sup>+0.87</sup> <sub>-0.89</sub>	1.03	0.63 <sup>+0.84</sup> <sub>-0.88</sub>	0.28
$f_{\text{err}}$	–	1.02 <sup>+0.05</sup> <sub>-0.13</sub>	1.08	0.98 <sup>+0.05</sup> <sub>-0.12</sub>	0.98	0.99 <sup>+0.05</sup> <sub>-0.11</sub>	0.99	0.98 <sup>+0.05</sup> <sub>-0.12</sub>	1.00
(*) $\sigma$	–	<0.013	0.002	<0.013	0.007	<0.012	0.006	<0.013	0.005
$a$	–	1.000 <sup>+0.001</sup> <sub>-0.001</sub>	1.000	1.000 <sup>+0.001</sup> <sub>-0.001</sub>	1.000	1.000 <sup>+0.001</sup> <sub>-0.001</sub>	1.000	1.000 <sup>+0.001</sup> <sub>-0.001</sub>	1.000
Goodness-of-fit at MLE									
$\chi^2$			1345		1375.1		1366.0		1340.5
$\chi^2_{\text{red}}$			1.002		1.029		1.022		1.003
$\log \mathcal{L}/N_{\text{DoF}}$			3.274		3.284		3.285		3.281
AIC			-8721.6		-8755.6		-8758.3		-8757.6
Diagnostics									
( <sup>(†)</sup> ) $N_{\text{step}}/\max(\tau_{\lambda})$			17		52		50		51
Acceptance rate			0.21		0.31		0.31		0.31
$N_{\text{DoF}}$			1335		1336		1336		1337

**Notes.** Unless stated otherwise, all parameters (except  $R_{\text{spec}}$ ) follow uniform priors. We describe the posterior distribution of any parameter by the median and the deviation of the 16th and 84th percentiles to the median. The maximum likelihood estimator (MLE) is given as well, at which point the goodness-of-fit diagnostics are determined. (\*)For  $\sigma$ , given the shape of the posterior distribution peaking close to 0 and compatible with 0 at less than  $2\text{-}\sigma$ , we only give the upper-limit at the 84th percentile. (<sup>(†)</sup>) $\max(\tau_{\lambda})$  is the maximum auto-correlation time among all varied parameters  $\lambda$ .

correction of  $8.1 \text{ km s}^{-1}$  this leads to a radial velocity of planet  $\beta \text{ Pic b}$  of  $8.7 \pm 0.9 \text{ km s}^{-1}$ . Compared to  $\beta \text{ Pic}$  systemic RV of  $\sim 20 \pm 0.7 \text{ km s}^{-1}$  (Gontcharov 2006), it implies an RV of the planet relative to  $\beta \text{ Pic}$ 's central star of  $-11.3 \pm 1.1 \text{ km s}^{-1}$  at MJD=56910.38. This value agrees at  $0.3\text{-}\sigma$  with the predicted RV of the planet at this MJD extrapolating the ephemerides of  $\beta \text{ Pic b}$ 's orbital motion from the RV+astro+imaging solution of Lacour et al. (2021) of  $-11.6 \text{ km s}^{-1}$ . It also compares well to the RV measured at high resolution using CRIRES a year earlier,  $-15.4 \pm 1.7 \text{ km s}^{-1}$  at MJD=56,644.5 (Snellen et al. 2014).

## 7. Discussion

### 7.1. A new estimation of $v \sin i$

In this work, we found a  $v \sin i$  of  $25^{+5}_{-6} \text{ km s}^{-1}$  in good agreement with the S14's result  $v \sin i = 25 \pm 3 \text{ km s}^{-1}$  and the most recent Landman et al. (2023)'s  $v \sin i$  estimation of  $19.9 \pm 1.1 \text{ km s}^{-1}$ . The larger confidence region of our measurement is explained by the much lower resolving power of SINFONI ( $R=4030 \pm 30$ , as determined in Sect. 2.4) compared to that of CRIRES ( $R=75\,000$ ).

S14 noticed that given the mass of the planet, the spin velocity of  $25 \text{ km s}^{-1}$  was too low to comply with the log-linear mass-spin law followed by Solar System objects from Jupiter down to asteroids (e.g. Hughes 2003), which would imply a spin

velocity of  $\sim 50 \text{ km s}^{-1}$ . Figure 20 shows this relationship for the Solar System planets, with a log-linear law that is well fitted to Earth+Moon<sup>5</sup>, Mars, Jupiter, Saturn, Uranus, and Neptune mass and equatorial speed, with values taken from Hughes (2003). Mercury and Venus are recognised as deviating from this law due to a loss of momentum during their lifetimes through tidal interactions with the Sun (Fish 1967; Burns 1975; Hughes 2003).

The difference in  $v \sin i$  for  $\beta \text{ Pic b}$  compared to the expected equatorial speed at a mass of  $\sim 11 M_J$  is mostly explained by the young age of the planet ( $\sim 23 \text{ Myr}$ ; Mamajek & Bell 2014). Indeed, the planet is currently contracting from  $\sim 1.5 R_J$  down to  $\sim 1 R_J$  (S14, Schwarz et al. 2016) and, thus, its spin should be accelerating. Figure 21 shows the effect of dilatation/contraction through time on the equatorial radius from two different evolution models: ATMO2020 (Phillips et al. 2020) and Baraffe-Chabrier-Barman (Baraffe et al. 2008). According to the conservation of momentum, its spin velocity is expected to increase up to  $40 \pm 20 \text{ km s}^{-1}$  at 4.5 Gyr, which is in better agreement with the Solar System law. Figure 22 shows the predicted  $v \sin i$  at 23 Myr evolved backward using the ATMO2020 models, down from an equatorial velocity determined by the spin-mass law at 4.5 Gyr shown in Fig. 20. In Fig. 22, it can

<sup>5</sup> Due to major exchange of momentum between Earth and Moon, the Earth+Moon couple is considered as if the Moon was put back into the Earth and the total momentum conserved (Hughes 2003).

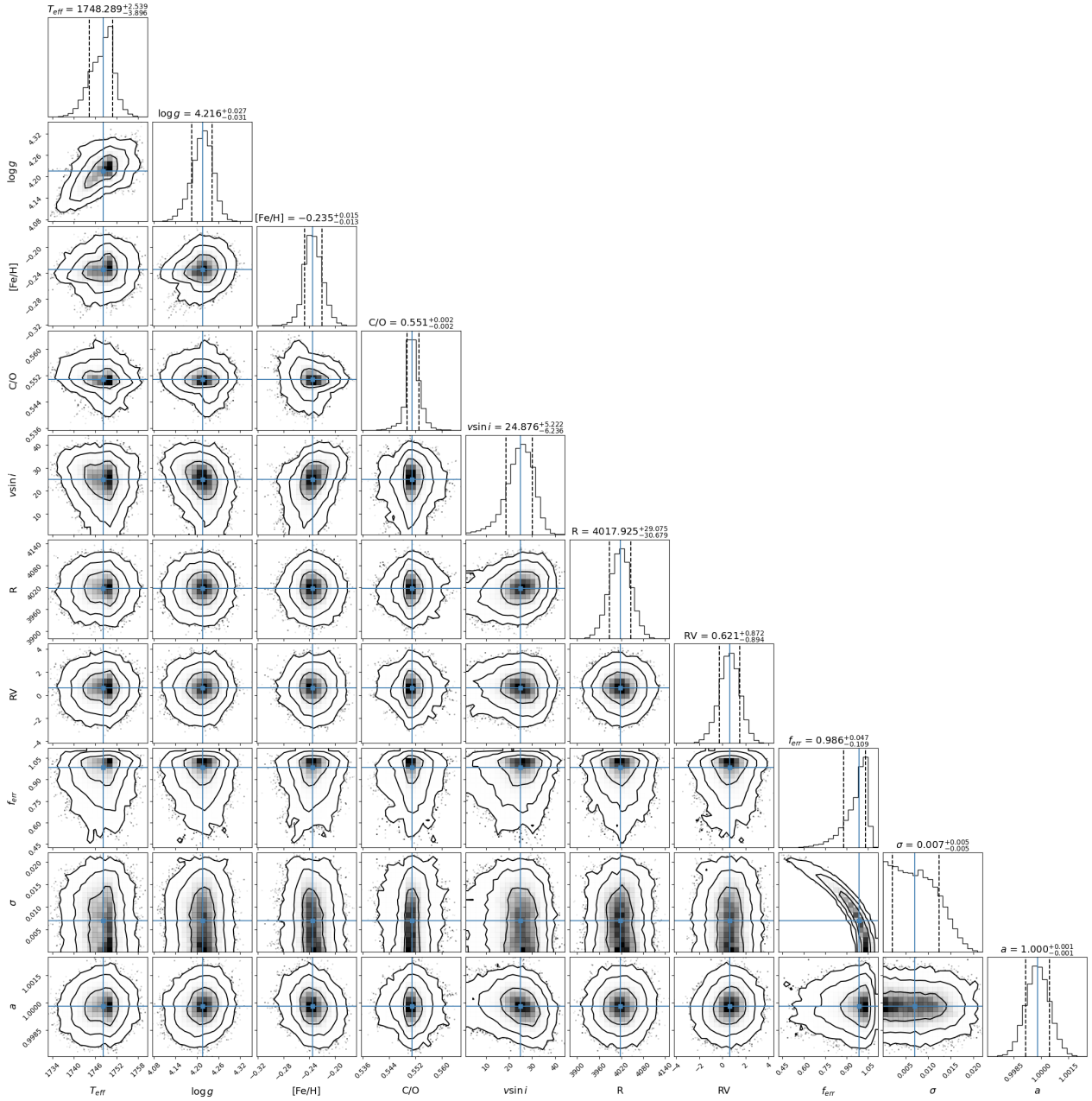


**Fig. 18.** Corner plot summarising the MCMC results for the fit of the  $\beta$  Pic b IR SINFONI spectrum by Exo-REM models with  $T_{\text{eff}}$  fixed at the [Chilcote et al. \(2017\)](#) value (see text for details).

be seen that even when we are taking into account the contraction, there is still a tension between the  $v \sin i$  measurements of  $\beta$  Pic b and its mass, especially if the mass is contained within 10–14  $M_J$ . The  $v \sin i$  and mass values overlap only over regions for  $v \sin i > 22 \text{ km s}^{-1}$ , with a mass of either  $< 10 M_J$  or  $> 14 M_J$ . These masses are marginally supported by the combined astrometric and RV measurements that favour a planetary mass within 9–15  $M_J$  ([Dupuy et al. 2019](#); [GRAVITY Collaboration 2020](#); [Lagrange et al. 2020](#); [Vandal et al. 2020](#); [Brandt et al. 2021](#); [Feng et al. 2022](#)).

This remaining discrepancy between mass and  $v \sin i$  could be explained by the random aspect of moment exchange during planet formation. However, it might also be the hint of a tilt of the planet’s equator compared to its orbital plane. In such case, the projected spin velocity,  $v \sin i$ , is smaller than the true equatorial

velocity. A direct compatibility at 1- $\sigma$  of the predicted  $v \sin i$  at 23 Myr for a mass at 11  $M_J$  and our measurement  $25 \pm 6 \text{ km s}^{-1}$  leads to a tilt compared to edge-on  $> 15^\circ$ .

## 7.2. A solar C/O

Here, we derive a value of the C/O for  $\beta$  Pic b that is Solar ( $0.551 \pm 0.002$ ), while [GRAVITY Collaboration \(2020\)](#) and [Landman et al. \(2023\)](#) found a sub-solar C/O of respectively  $0.43 \pm 0.05$  and  $0.41 \pm 0.04$ . Forming  $\beta$  Pic b in situ along the core accretion scenario ([Pollack et al. 1996](#)) would imply a C/O ratio in the atmosphere of the planet largely super-solar  $> 0.8$ , because of the expected abundances of the different gases in the disk from one ice line to the other when assuming a disk with a static composition all through the main phase of planet formation



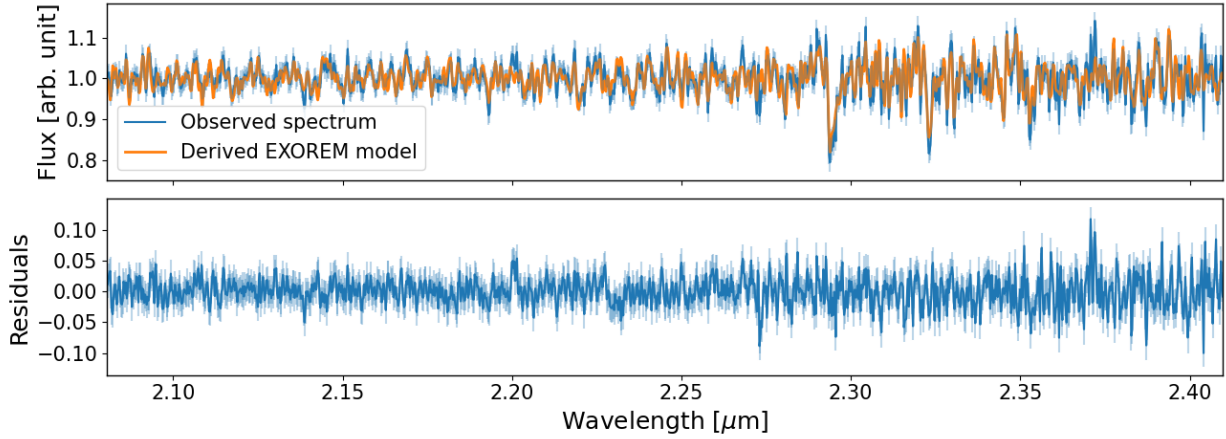


**Fig. 19.** Plot comparing in the top-panel the  $\beta$  Pic b SINFONI spectrum (blue) and the median Exo-REM model (orange) from the MCMC posteriors with  $T_{\text{eff}}$  fixed at the Chilcote et al. (2017)’s value (see text). The bottom-panel shows the residuals. The uncertainties assumed for the observed flux are plotted as light-blue vertical lines.

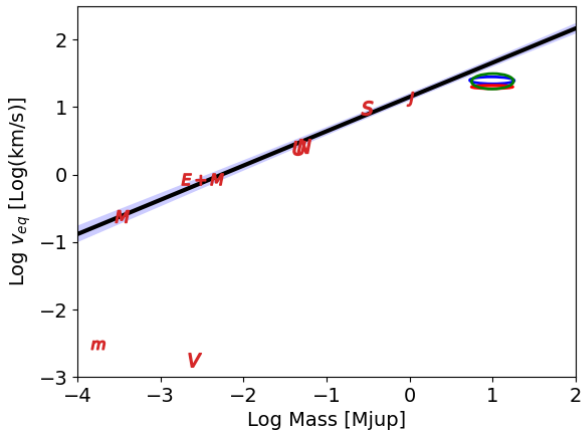


**Fig. 20.** Log-linear relationship between the equatorial velocity and mass of Solar System planets. In blue: possible laws compatible with planets Mars, Jupiter, Saturn, Uranus, and Neptune. The ellipses show the  $v \sin i$  and mass of  $\beta$  Pic b derived in this work (pink), in S14 (cyan), and Landman et al. (2023, red).

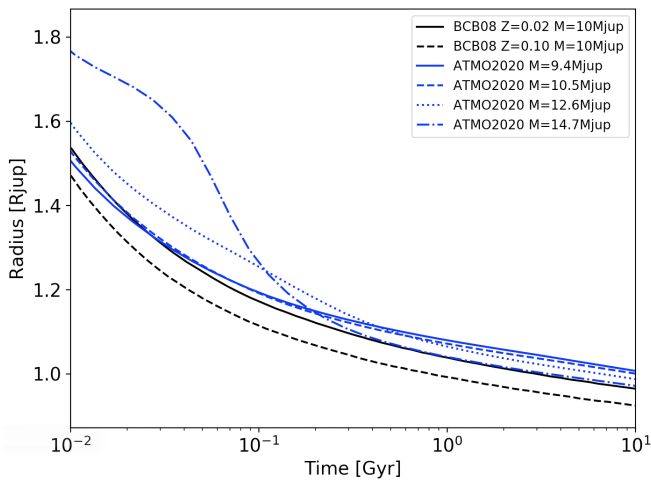


**Fig. 21.** Illustration of evolutionary tracks of equatorial radius through time with ATMO2020 models (Phillips et al. 2020) and Baraffe–Chabrier–Barman (Baraffe et al. 2008) or BCB08 models at different planet mass.

(Öberg et al. 2011). In this framework, a proposed scenario for reaching solar and sub-solar C/O is to consider the accretion of icy planetesimals from beyond the ice lines, where most of the  $\text{H}_2\text{O}$  and  $\text{CO}_2$  of the disk is in condensed phase. Alternatively, a solar C/O is more naturally reached by forming either by gravitational instability (Boss 1997) anywhere in the disk or by core accretion close to the  $\text{H}_2\text{O}$  ice line with a moderate planetesimal accretion followed by an outward migration. Given that core accretion is preferred for most compact planetary systems with also terrestrial planets (as in e.g. the Solar System) and that the  $\beta$  Pic system has at least two planets, with one within 5 au (Lagrange et al. 2019) plus small km-sized icy bodies (Ferlet et al. 1987; Beust et al. 1990; Kiefer et al. 2014; Lecavelier des Etangs et al. 2022), we further consider this scenario as the most likely for forming the  $\beta$  Pic’s planets.

In this framework, we can estimate the location of the ice lines compared to  $\beta$  Pic b location in the disk. Following Öberg et al. (2011), the typical temperature profile in a protoplanetary disk is given by (Andrews & Williams 2005, 2007):

$$T = T_0 \left( \frac{r}{1 R_\star} \right)^{-0.62}. \quad (11)$$

Here,  $T_0$  is the average temperature in the disk as if it were located at  $1 R_\star$  from the centre of the star. Given the effective temperature of  $\beta$  Pic (Saffe et al. 2021), we have that  $T_0=8000$  K. Considering the typical evaporation temperatures of  $\text{H}_2\text{O}$ ,  $\text{CO}_2$ , and CO summarised in Table 5 with  $R_\star=1.7 R_\odot$  (Kervella et al. 2004), we derived the radii of the different ice lines around  $\beta$  Pic (also shown in Table 5). We find that with  $a_b \sim 9.8$  au (Lagrange et al. 2020), planet b is located between the  $\text{H}_2\text{O}$  ( $6 \pm 1$  au) and the  $\text{CO}_2$  ( $31 \pm 5$  au) ice lines. Figure 23 shows the variation of the ice lines through time, as derived using Dartmouth12 evolutionary tracks for pre-main sequence stars.

Following Petrus et al. (2021), our C/O measurement fits well to the Nissen (2013) planet-C/O to star-Fe/H linear relation. They indeed reported a positive correlation between the C/O ratio and the [Fe/H] of stars with an average  $\text{C/O}=0.58 \pm 0.06$  at [Fe/H]=0. Elemental abundances and spectral matching agree on a metallicity of  $\beta$  Pic that is solar up to a factor  $\sim 2$  (Holweger et al. 1997). Our C/O of  $0.551^{+0.003}_{-0.002}$  is in good agreement with the expected solar C/O for a solar metallicity. The low metallicity of the planet that we found,  $-0.235^{+0.015}_{-0.013}$ ,

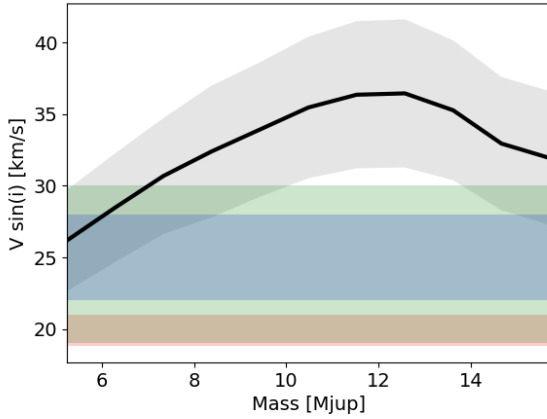


**Fig. 22.**  $v \sin i$  prediction (gray region and black solid line) of the planet for different masses at 23 Myr, assuming a tilt of  $0^\circ$  compared to edge-on. Green and blue area show the  $v \sin i$  confidence regions on  $\beta$  Pic b based on this work and the results from S14 (blue) and (Landman et al. 2023; red).

**Table 5.** Ice lines of CO, CO<sub>2</sub>, and H<sub>2</sub>O.

Molecule	$T_{\text{evap}}$ (K)	$r_{\text{ice}}$ (au)
CO	$20 \pm 2$	$125 \pm 20$
CO <sub>2</sub>	$47 \pm 5$	$31 \pm 5$
H <sub>2</sub> O	$135 \pm 15$	$5.7 \pm 1.0$

**Notes.** The values of  $T_{\text{evap}}$  are taken from Öberg et al. (2011) and the corresponding ice lines radii are calculated as explained in the text.

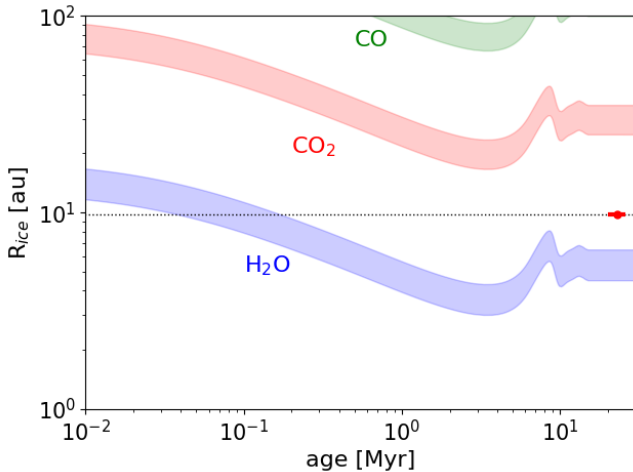


**Fig. 23.** Ice lines locations through time of H<sub>2</sub>O, CO<sub>2</sub>, and CO derived for  $\beta$  Pictoris. The location of planet *b* is marked as a red circle at  $23 \pm 3$  Myr and prolonged down to 10 kyr with a black dotted line.

is also in agreement with new-generation planetary population synthesis (NGPPS, Schlecker et al. 2021) simulations through core-accretion, on the same range of semi-major axis  $\sim 10$  au, especially if the mass of  $\beta$  Pic b is larger than  $10 M_J$ . The correlation between bulk metallicity and planet mass, as obtained through the NGPPS simulations performed around stellar hosts with metallicities ranging from  $-0.5$  to  $0.5$ , as seen in Fig. 10 of Petrus et al. (2021).

To explain the C/O value found when assuming a static disk composition during planet formation, as in Öberg et al. (2011),

we propose that: i) planets b and c underwent an inner migration during the first Myr of their formation, allowing them to gather large amounts of gas with a solar composition; this is followed by ii) an outward migration, with planet b and c in a 7:1 mean motion resonance leading them to reach their actual location (Beust et al., priv. comm.). This scenario would allow us to avoid fine-tuning the icy planetesimal accretion within the planet to reach a nearly ideal solar C/O.

Alternatively, there is a scenario that does not require us to invoke an outward migration for  $\beta$  Pic b. Considering non-static disk composition, Mollière et al. (2022) found that pebble evaporation and the dilution of water and CO in-between the H<sub>2</sub>O and CO iceline (Fig. 6 in Mollière et al. 2022) can lead to a nearly stellar C/O ratio in the circumstellar gas in about 1 Myr. That could enable the in situ formation of  $\beta$  Pic b, provided most of its gas had not been accreted before 1 Myr.

In summary, a solar C/O for  $\beta$  Pic b is challenging for planet formation models. Interestingly, it fits into the mass-C/O relation obtained by Hoch et al. (2022). These authors found a clear threshold at  $4 M_J$ , beyond which imaged planet mostly have C/O consistent with solar  $\sim 0.55$ ; whereas below  $4 M_J$ , a transiting planet a C/O value from 0.2 to 2.0. This threshold has been interpreted as distinguishing two main formation pathways for planets that are either less massive than  $4 M_J$  and or more massive than  $4 M_J$ . This  $4 M_J$  threshold was already reported with respect to the distribution of stellar metallicities among massive giant exoplanets, offering a similar interpretation (Santos et al. 2017). Therefore, the solar C/O of  $\beta$  Pic b might be the sign of a formation scenario that differs from the usual core accretion scenario invoked for close-in less massive planets; namely, it still includes core accretion, but considering perhaps a distinct pathway for planets formed at large separation that did not undergo inward migration or, more simply, by gravitational instability.

## 8. Conclusion

In this study, we have derived a new infrared spectrum of the young giant planet  $\beta$  Pic b observed with SINFONI. We have shown that the actual spectral resolving power of SINFONI in the *K*-band at a spaxel-resolution of  $12.5 \times 25 \text{ mas}^2$  is  $\sim 4000$ . Then, using a novel method of stellar halo removal, we have been able to directly extract the spectrum and the molecular lines of the planet without the need of using molecular mapping techniques. We have fitted the spectrum to models from the forward-modeling Exo-REM library. This has led to different results, depending on assumptions on the planet mass and radius:

- without any prior constraints, we obtained  $T_{\text{eff}} = 1555^{+22}_{-29}$  K at a  $\log g = 3.12^{+0.12}_{-0.09}$ , with a sub-solar metallicity of  $-0.325^{+0.065}_{-0.045}$  dex and a super-solar C/O =  $0.79^{+0.01}_{-0.11}$ ,
- assuming a prior on the  $T_{\text{eff}} = 1724 \pm 15$  K, based on an independent photometric characterisation from Chilcote et al. (2017), we found a higher  $T_{\text{eff}} = 1748^{+3}_{-4}$  K, again with a sub-solar metallicity of  $-0.235^{+0.015}_{-0.013}$  dex and a now solar C/O =  $0.551 \pm 0.002$ .

Our preferred parameters were derived imposing  $T_{\text{eff}} = 1724 \pm 15$  K, as this better reflects the gravitational mass and the geometric radius derived independently using photometry. We found a projected rotation speed of  $\beta$  Pic b's equator of  $25^{+5}_{-6} \text{ km s}^{-1}$  agreeing with the  $25 \pm 3 \text{ km s}^{-1}$  found by Snellen et al. (2014) at high spectral resolution with CRIRES and the most recent CRIRES+ Landman et al. (2023)'s  $v \sin i = 19.9 \pm 1.1 \text{ km s}^{-1}$ . However, our measurement of a solar C/O is in stark contrast

with the sub-solar C/O $\sim$ 0.45 obtained from GRAVITY spectra (GRAVITY Collaboration 2020) and by the atmospheric retrieval of CRILES spectra in Landman et al. (2023).

Conversely to the conclusions of GRAVITY Collaboration (2020), with a C/O for the star also close to 0.55, the stellar C/O disfavors the scenario of icy-planetesimals injection. It would indeed imply the need to fine-tune the planetesimals' accretion flux and of the duration of the phenomenon, so that it reaches a value close to the stellar C/O. Such a value of  $\beta$  Pic b's C/O is, on the other hand, in better agreement with in situ gravitational instability scenario or formation next to the H<sub>2</sub>O ice line, followed by migration. This latter scenario could be supported by the proximity of the planets b & c orbital periods to a 7:1 resonance, whose orbital parameters may have significantly evolved during the first Myrs of the system.

Finally, we measured a radial velocity of  $\beta$  Pic b relative to the central star of  $-11.3 \pm 1.1$  km s<sup>-1</sup> at MJD=56,910.38. This is in agreement, at 0.3- $\sigma$ , with the ephemerides for the orbit of this planet based on the current knowledge of the system from (Lacour et al. 2021). This tends to confirm the current estimation of the orbits and mass of the  $\beta$  Pic's planets, while adding a new RV point for future dynamical characterisations of the system.

The present work shows that ground-based infrared medium-resolution spectroscopy with even a modest resolving power of 4000 (close to that of the JWST/MIRI-MRS) without the need to carry out molecular mapping and with a careful treatment of wavelength calibration, as well as star halo and telluric lines subtraction at any wavelengths. This can allow for the derivation of key properties of imaged exoplanets, including the equatorial rotation velocity. Proper determinations of the atmospheric parameters still requires independent priors, such as on  $T_{\text{eff}}$  or  $\log g$ , due to the fit degeneracy of the unresolved spectral lines.

*Acknowledgements.* We are thankful to Alain Smette for his careful and constructive reading of the manuscript that helped improving the analysis significantly. This work was granted access to the HPC resources of MesoPSL financed by the Region Ile de France and the project EquipMeso (reference ANR-10-EQPX-29-01) of the programme Investissements d'Avenir supervised by the Agence Nationale pour la Recherche. This project has received funding from the European Research Council (ERC) under the European Union's Horizon 2020 research and innovation programme (COBREX; grant agreement no. 885593). This work was also funded by the initiative de recherches interdisciplinaires et stratégiques (IRIS) of Université PSL "Origines et Conditions d'Apparition de la Vie (OCAV)". F.K. also acknowledges funding from the Action Incitative Exoplanètes de l'Observatoire de Paris.

## References

- Andrews, S. M., & Williams, J. P. 2005, *ApJ*, 631, 1134  
 Andrews, S. M., & Williams, J. P. 2007, *ApJ*, 659, 705  
 Asplund, M., Grevesse, N., Sauval, A. J., & Scott, P. 2009, *ARA&A*, 47, 481  
 Baraffe, I., Chabrier, G., & Barman, T. 2008, *A&A*, 482, 315  
 Baudino, J. L., Bézard, B., Boccaletti, A., et al. 2015, *A&A*, 582, A83  
 Beust, H., Lagrange-Henri, A. M., Vidal-Madjar, A., & Ferlet, R. 1990, *A&A*, 236, 202  
 Birkby, J. L., de Kok, R. J., Brogi, M., et al. 2013, *MNRAS*, 436, L35  
 Birkby, J. L., de Kok, R. J., Brogi, M., Schwarz, H., & Snellen, I. A. G. 2017, *AJ*, 153, 138  
 Blain, D., Charnay, B., & Bézard, B. 2021, *A&A*, 646, A15  
 Bonnefoy, M., Boccaletti, A., Lagrange, A. M., et al. 2013, *A&A*, 555, A107  
 Bonnet, H., Abuter, R., Baker, A., et al. 2004, *The Messenger*, 117, 17  
 Boss, A. P. 1997, *Science*, 276, 1836  
 Brandt, G. M., Brandt, T. D., Dupuy, T. J., Li, Y., & Michalik, D. 2021, *AJ*, 161, 179  
 Brogi, M., Snellen, I. A. G., de Kok, R. J., et al. 2012, *Nature*, 486, 502  
 Brogi, M., Snellen, I. A. G., de Kok, R. J., et al. 2013, *ApJ*, 767, 27  
 Brogi, M., de Kok, R. J., Birkby, J. L., Schwarz, H., & Snellen, I. A. G. 2014, *A&A*, 565, A124  
 Brogi, M., Giacobbe, P., Guilluy, G., et al. 2018, *A&A*, 615, A16  
 Burns, J. A. 1975, *Icarus*, 25, 545  
 Charnay, B., Bézard, B., Baudino, J. L., et al. 2018, *ApJ*, 854, 172  
 Chilcote, J., Pueyo, L., De Rosa, R. J., et al. 2017, *AJ*, 153, 182  
 Cont, D., Yan, F., Reiners, A., et al. 2021, *A&A*, 651, A33  
 Cont, D., Yan, F., Reiners, A., et al. 2022a, *A&A*, 668, A53  
 Cont, D., Yan, F., Reiners, A., et al. 2022b, *A&A*, 657, L2  
 Cugno, G., Patapis, P., Stolker, T., et al. 2021, *A&A*, 653, A12  
 de Kok, R. J., Brogi, M., Snellen, I. A. G., et al. 2013, *A&A*, 554, A82  
 Demars, D., Bonnefoy, M., Dougados, C., et al. 2023, *A&A*, 676, A123  
 Dupuy, T. J., Brandt, T. D., Kratter, K. M., & Bowler, B. P. 2019, *ApJ*, 871, L4  
 Eisenhauer, F., Abuter, R., Bickert, K., et al. 2003, *SPIE Conf. Ser.*, 4841, 1548  
 Feng, F., Butler, R. P., Vogt, S. S., et al. 2022, *ApJS*, 262, 21  
 Ferlet, R., Hobbs, L. M., & Vidal-Madjar, A. 1987, *A&A*, 185, 267  
 Fish, F. F. 1967, *Icarus*, 7, 251  
 Foreman-Mackey, D., Hogg, D. W., Lang, D., & Goodman, J. 2013, *PASP*, 125, 306  
 Gontcharov, G. A. 2006, *Astron. Astrophys. Trans.*, 25, 145  
 GRAVITY Collaboration (Nowak, M., et al.) 2020, *A&A*, 633, A110  
 Gray, D. F. 1997, *High resolution spectroscopy, in Instrumentation for large telescopes*, 163  
 Guilluy, G., Sozzetti, A., Brogi, M., et al. 2019, *A&A*, 625, A107  
 Hoch, K. K. W., Konopacky, Q. M., Theissen, C. A., et al. 2023, *ApJ*, 166, 85  
 Hoeijmakers, H. J., Schwarz, H., Snellen, I. A. G., et al. 2018, *A&A*, 617, A144  
 Holweger, H., Hempel, M., van Thiel, T., & Kaufer, A. 1997, *A&A*, 320, L49  
 Hughes, D. W. 2003, *Planet. Space Sci.*, 51, 517  
 Kausch, W., Noll, S., Smette, A., et al. 2015, *A&A*, 576, A78  
 Kervella, P., Thévenin, F., Morel, P., et al. 2004, in *Stars as Suns: Activity, Evolution and Planets*, eds. A. K. Dupree, & A. O. Benz, 219, 80  
 Kervella, P., Arenou, F., Mignard, F., & Thévenin, F. 2019, *A&A*, 623, A72  
 Kervella, P., Arenou, F., & Thévenin, F. 2022, *A&A*, 657, A7  
 Kiefer, F., Lecavelier des Etangs, A., Boissier, J., et al. 2014, *Nature*, 514, 462  
 Lacour, S., Wang, J. J., Rodet, L., et al. 2021, *A&A*, 654, A2  
 Lagrange, A. M., Gratadour, D., Chauvin, G., et al. 2009, *A&A*, 493, L21  
 Lagrange, A. M., Bonnefoy, M., Chauvin, G., et al. 2010, *Science*, 329, 57  
 Lagrange, A. M., Boccaletti, A., Milli, J., et al. 2012, *A&A*, 542, A40  
 Lagrange, A. M., Meunier, N., Rubini, P., et al. 2019, *Nat. Astron.*, 3, 1135  
 Lagrange, A. M., Rubini, P., Nowak, M., et al. 2020, *A&A*, 642, A18  
 Landman, R., Stolker, T., Snellen, I., et al. 2023, *A&A*, 682, A48  
 Lecavelier des Etangs, A., Cros, L., Hébrard, G., et al. 2022, *Sci. Rep.*, 12, 5855  
 Lockwood, A. C., Johnson, J. A., Bender, C. F., et al. 2014, *ApJ*, 783, L29  
 Málin, M., Boccaletti, A., Charnay, B., Kiefer, F., & Bézard, B. 2023, *A&A*, 671, A109  
 Mamajek, E. E., & Bell, C. P. M. 2014, *MNRAS*, 445, 2169  
 Marois, C., Lafrenière, D., Doyon, R., Macintosh, B., & Nadeau, D. 2006, *ApJ*, 641, 556  
 Mesa, D., Gratton, R., Kervella, P., et al. 2023, *A&A*, 672, A93  
 Miles, B. E., Biller, B. A., Patapis, P., et al. 2023, *ApJ*, 946, L6  
 Mollière, P., Molyarova, T., Bitsch, B., et al. 2022, *ApJ*, 934, 74  
 Morzinski, K. M., Males, J. R., Skemer, A. J., et al. 2015, *ApJ*, 815, 108  
 Nissen, P. E. 2013, *A&A*, 552, A73  
 Nowak, M., Lacour, S., Lagrange, A. M., et al. 2020, *A&A*, 642, A2  
 Öberg, K. I., Murray-Clay, R., & Bergin, E. A. 2011, *ApJ*, 743, L16  
 Palma-Bifani, P., Chauvin, G., Bonnefoy, M., et al. 2023, *A&A*, 670, A90  
 Patapis, P., Nasedkin, E., Cugno, G., et al. 2022, *A&A*, 658, A72  
 Petit dit de la Roche, D. J. M., Hoeijmakers, H. J., & Snellen, I. A. G. 2018, *A&A*, 616, A146  
 Petrus, S., Bonnefoy, M., Chauvin, G., et al. 2021, *A&A*, 648, A59  
 Petrus, S., Chauvin, G., Bonnefoy, M., et al. 2023, *A&A*, 670, A9  
 Phillips, M. W., Tremblin, P., Baraffe, I., et al. 2020, *A&A*, 637, A38  
 Piskorz, D., Benneke, B., Crockett, N. R., et al. 2016, *ApJ*, 832, 131  
 Piskorz, D., Benneke, B., Crockett, N. R., et al. 2017, *AJ*, 154, 78  
 Pollack, J. B., Hubickyj, O., Bodenheimer, P., et al. 1996, *Icarus*, 124, 62  
 Ruffio, J.-B., Macintosh, B., Konopacky, Q. M., et al. 2019, *AJ*, 158, 200  
 Ruffio, J.-B., Konopacky, Q. M., Barman, T., et al. 2021, *AJ*, 162, 290  
 Saffe, C., Miquelarena, P., Alacoria, J., et al. 2021, *A&A*, 647, A49  
 Santos, N. C., Adibekyan, V., Figueira, P., et al. 2017, *A&A*, 603, A30  
 Schlecker, M., Mordasini, C., Emsenhuber, A., et al. 2021, *A&A*, 656, A71  
 Schwarz, H., Ginski, C., de Kok, R. J., et al. 2016, *A&A*, 593, A74  
 Skilling, J. 2006, *Bayesian Anal.*, 1, 833  
 Smette, A., Sana, H., Noll, S., et al. 2015, *A&A*, 576, A77  
 Snellen, I. A. G., & Brown, A. G. A. 2018, *Nat. Astron.*, 2, 883  
 Snellen, I. A. G., Brandl, B. R., de Kok, R. J., et al. 2014, *Nature*, 509, 63  
 Tamuz, O., Mazeh, T., & Zucker, S. 2005, *MNRAS*, 356, 1466  
 Vandal, T., Rameau, J., & Doyon, R. 2020, *AJ*, 160, 243  
 Yan, F., Pallé, E., Reiners, A., et al. 2022, *A&A*, 661, A6

## Appendix A: MCMC run with all free parameters

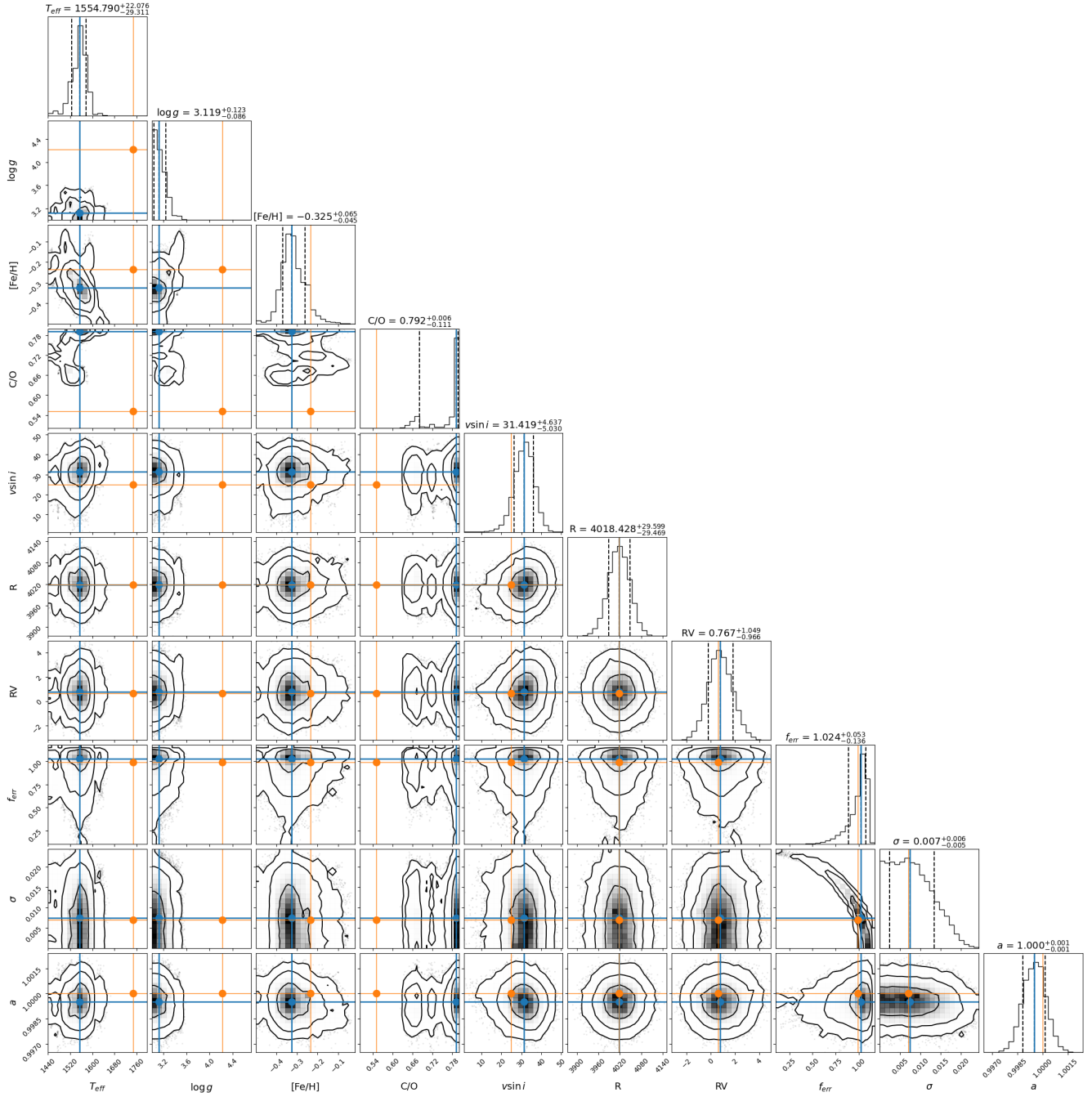


**Fig. A.1.** Corner plot summarising the MCMC results for the fit of the  $\beta$  Pic b IR SINFONI spectrum by Exo-REM models with all free parameters. The blue lines and dot show the median parameters. The orange lines and dot are those found for the preferred solution (see Section 6.2).

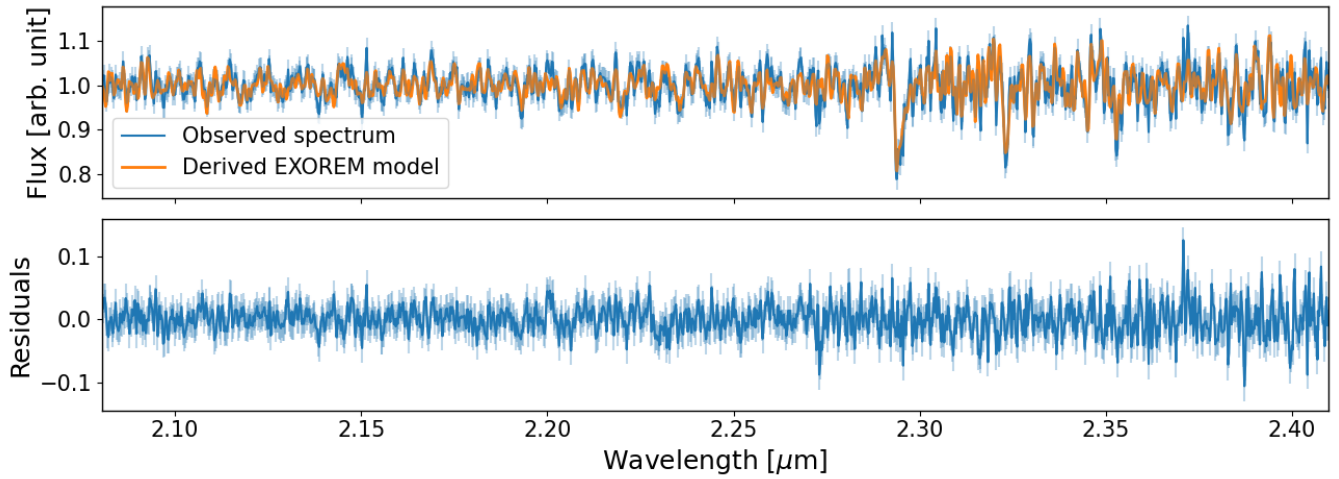


**Fig. A.2.** Plot comparing the  $\beta$  Pic b SINFONI spectrum (blue) and the median Exo-REM model (orange) from the MCMC posteriors (Fig. A.1). The lower panel shows the residuals. The uncertainties assumed for the observed flux are plotted as light-blue vertical lines.